THESIS FOR THE DEGREE OF DOCTOR OF PHILOSOPHY

3D-Printing of Fluorinated Polymer-based Materials for Plasmonic Sensing

IDA ÖSTERGREN

Department of Chemistry and Chemical Engineering

CHALMERS UNIVERSITY OF TECHNOLOGY

Gothenburg, Sweden 2023

3D-Printing of Fluorinated Polymer-based Materials for Plasmonic Sensing

IDA ÖSTERGREN

ISBN 978-91-7905-953-8

Doktorsavhandlingar vid Chalmers tekniska högskola
Ny serie nr 5419
ISSN 0346-718X

Department of Chemistry and Chemical Engineering
Chalmers University of Technology
SE-412 96 Gothenburg
Sweden
Telephone + 46 (0)31-772 1000

Cover:
Photograph of 3D-printed miniature version of the Vinga lighthouse and beacon made with PMMA:Au composite. Photography by Malin Arnesson/Chalmers.

Chalmers Digitaltryck
Gothenburg, Sweden 2023

3D-Printing of Fluorinated Polymer-based Materials for Plasmonic Sensing

IDA ÖSTERGREN
Department of Chemistry and Chemical Engineering
Chalmers University of Technology

ABSTRACT

Hydrogen attracts growing interest as a versatile energy carrier, serving as a fuel for cars, a heat source, or a reagent for chemical synthesis. At the same time, the demand for accurate and selective hydrogen sensors is increasing, because of both safety concerns and the need for process monitoring. This thesis discusses plasmonic sensors as a viable option for hydrogen sensing and in particular the transition from 2D thin films to bulk production of plasmonic plastic nanocomposites via melt processing and 3D-printing. This thesis explores a processing methodology that has the potential to produce a broad range of plasmonic plastic nanocomposites, by allowing for variation in both the type of nanoparticles and the polymer matrix.

First, different Au nanoparticles were compounded together with poly(lactic acid) (PLA) and poly(methyl methacrylate) (PMMA) and 3D-printed to demonstrate the versatility and processability of plasmonic plastic nanocomposites. Secondly, Pd- and PdAu based composites with PMMA and Teflon AF as the polymer matrix were produced to create 3D-printed plasmonic hydrogen sensors. Furthermore, the hydrogen sensing kinetics and protective properties of the polymer matrix surrounding the Pd nanoparticles were evaluated. The use of PMMA:Pd nanocomposites resulted in a robust sensor, that offers good protection against carbon monoxide poisoning. Whilst, Teflon AF:Pd nanocomposites facilitate fast sensing due to a high hydrogen diffusivity. To combine the advantages of both matrix polymers, a core:shell approach with a Teflon AF:Pd nanocomposite as the bulk material and PMMA as a surface coating is explored. This approach yields a sensor with a promising degree of carbon monoxide protection, without affecting the fast sensor response of the Teflon AF:Pd nanocomposite. Evidently, the use of polymer nanocomposites is a promising avenue for the realization of fast and selective hydrogen sensors.

Keywords: hydrogen sensing, plasmonic nanoparticles, polymer nanocomposite, 3D-printing, fused deposition modeling, Teflon AF

Acknowledgement

I would like to take the opportunity to thank my supervisor Christian Müller for employing me at such an early stage and for insisting that this would be a PhD project that would suit me well. For me, you have been such a great supervisor and manager, always staying positive, having my back, and supporting me both scientific and in general.

Thanks to everyone in the plasmonic plastics project: Iwan Darmadi, Alicja Stolas, Robson da Silva, Magnus Rahm, Lucy Cusinato, Christoph Langhammer, Kasper Moth-Poulsen, Paul Erhart and Anders Hellman. It has been a pleasure to work with all of you. This project could not have been done without you.

I would also like to thank the people outside of Chalmers that have helped and collaborated with me during this thesis: Matteo Minelli and Giacomo Foli at University of Bologna, Marianne Liebe at PSI, Saima Zama at Insplorion and Massimo Macaroni at Gothenburg University.

A special thanks to Anja and Anna H for pushing and motivating me when things were tough but mainly for showing me how great it is to do science in an all-women's team. To Amir for stepping in and continuing my work while I was on parental leave. To Jonna and Sarah, for always taking a morning coffee with me and having an open ear whenever I needed to get something off my chest. To Lotta, for making floor 8th the best floor at Chalmers.

I would like to thank all my previous and recent colleagues in the Müller group and at floor 8th. You have all made Chalmers the best place to work at and I can only hope to have as amazing colleagues as you in the future.

To my mum, dad, and sister, for all your support and love. For helping me to take rest when I need it and for pointing out what really is important in life. To all my friends, especially Linn, Hilda and Astrid, thanks for all the fun, for all the nice talks and for trying to figure out how to balance life, work, and motherhood.

To my family, I love you all. I would not have done this without you Martin. Thanks for all the support and motivation, for always being on my side and for all the vab you have been taking this fall. To Malte and Hjalmar, you are my sunshine, and you make it so easy for me to take my mind off work. Thank you for being so active, energetic, and full of life and love.

Nomenclature

A	Membrane area
ABS	Acrylonitrile butadiene styrene
CAD	Computer aided design
CH_4	Methane
CO	Carbon monoxide
CTAB	Hexadecyltrimethylammonium bromide
De	The Deborah number
D	Diffusivity
E	Elastic modulus
ε	Optical extinction
$\Delta\bar{\varepsilon}_{max}$	Maximum sensor response
FDM	Fused deposition modeling
FFV	Fractional free volume
g-code	Geometric code
H_2	Hydrogen
HDT	Heat deflection temperature
HIPS	High impact polystyrene
IEA	International Energy Agency
J_{ss}	Penetrant molar flux per unit area at steady state
η	Melt viscosity
NO_x	Nitrogen oxide
NP	Nanoparticle
P	Permeability
Δp	Pressure difference
p_d	Downstream pressure
PA6	Polyamide 6

PBF	Powder bed fusion
PdH	Palladium hydride
PE	Polyethylene
PLA	Poly(lactic acid)
PMMA	Poly(methyl methacrylate)
PTFE	Poly(tetrafluoroethylene)
PVDF	Poly(vinylidene fluoride)
PVP	Polyvinylpyrrolidone
Q	Quality factor
S	Solubility
SLA	Stereolithography
SLS	Selective laser sintering
SO_x	Sulphur oxide
SSF	Swedish Foundation of Strategic research
TEM	Transmission electron microscopy
Θ_L	Time-lag value
T_m	Melt temperature
T_g	Glass transition temperature
$t_{50,resp}$	Response time
$t_{50,rec}$	Recovery time
UVVis	Ultraviolet visible
V_d	Calibrated volume of the downstream chamber

List of Publications

This thesis consist of an extended summary and the following appended papers:

Paper I **Bulk-Processed Pd Nanocube–Poly(methyl methacrylate) Nanocomposites as Plasmonic Plastics for Hydrogen Sensing**

Iwan Darmadi, Alicja Stolaś, Ida Östergren, Barbara Berke, Ferry Anggoro Ardy Nugroho, Matteo Minelli, Sarah Lerch, Irem Tanyeli, Anja Lund, Olof Andersson, Vladimir P. Zhdanov, Marianne Liebi, Kasper Moth-Poulsen, Christian Müller, and Christoph Langhammer

ACS Appl. Nano Mater. 2020, 3, 8, 8438–8445

Paper II **Highly Permeable Fluorinated Polymer Nanocomposites for Plasmonic Hydrogen Sensing**

Ida Östergren, Amir Masoud Pourrahimi, Iwan Darmadi, Robson da Silva, Alicja Stolaś, Sarah Lerch, Barbara Berke, Manuel Guizar-Sicairos, Marianne Liebi, Giacomo Foli, Vincenzo Palermo, Matteo Minelli, Kasper Moth-Poulsen, Christoph Langhammer, and Christian Müller

ACS Appl. Mater. Interfaces 2021, 13, 18, 21724–21732

Paper III **A Surface Passivated Fluorinated Polymer Nanocomposite for Carbon Monoxide Resistant Plasmonic Hydrogen Sensing**

Ida Östergren, Iwan Darmadi, Robson da Silva, Sarah Lerch, Kasper Moth-Poulsen, Christoph Langhammer and Christian Müller

Submitted

Paper IV **Bulk-Processed Plasmonic Plastic Nanocomposite Materials for Optical Hydrogen Detection**

Iwan Darmadi, Ida Östergren, Sarah Lerch, Anja Lund, Kasper Moth-Poulsen, Christian Müller, Christoph Langhammer

Acc. Chem. Res. 2023, 56, 13, 1850–1861

Contribution report

Paper I Shared main author. Responsible for design of experiments and material planning together with I.D and A.S. Compounded, melt-pressed and 3D-printed all of the nanocomposites. Executed the elemental analysis. Data analysis together with I.D and A.S. Assisted during the writing of the paper.

Paper II Shared main author. Responsible for concept of the work and the design of experiments. Compounded, melt-pressed and 3D-printed all of the nanocomposites. Executed the elemental analysis. Data analysis and interpretation together with I.D and A.M.P. Revised the manuscript together with all co-authors.

Paper III Main author. Responsible for concept of the work and the design of experiments. Compounded and melt-pressed the nanocomposite. Dip-coating together with S.L. FTIR analysis together with S.L. Data analysis and interpretation together with I.D. Compiled the data and wrote the first draft of the manuscript together with C.M.

Paper IV Co-author. Responsible for the design of experiments regarding nanocomposites. Compounded, melt-pressed and 3D-printed all of the small-scale Au nanocomposites. Compounded and melt-pressed Teflon AF:PdAu together with S.L. Responsible for up-scaling of nanocomposite together with A.L Assisted during the writing of the paper.

Publications not included in this thesis

Paper V **Dynamic Nanocellulose Networks for Thermoset-like yet Recyclable Plastics with a High Melt Stiffness and Creep Resistance**

Anna Peterson, Ida Östergren, Antiope Lotsari, Abhijit Venkatesh, Johannes Thunberg, Anna Ström, Ramiro Rojas, Martin Andersson, Lars A. Berglund, Antal Boldizar, and Christian Müller

Biomacromolecules 2019, 20, 10, 3924–3932

Paper VI **All-Polymer Conducting Fibers and 3D Prints via Melt Processing and Templated Polymerization**

Anna I. Hofmann, Ida Östergren, Youngseok Kim, Sven Fauth, Mariavittoria Craighero, Myung-Han Yoon, Anja Lund, and Christian Müller

ACS Appl. Mater. Interfaces 2020, 12, 7, 8713–8721

Paper VII **Recyclable Polyethylene Insulation via Reactive Compounding with a Maleic Anhydride-Grafted Polypropylene**

Yingwei Ouyang, Massimiliano Mauri, Amir Masoud Pourrahimi, Ida Östergren, Anja Lund, Thomas Gkourmpis, Oscar Prieto, Xiangdong Xu, Per-Ola Hagstrand, and Christian Müller

ACS Appl. Polym. Mater. 2020, 2, 6, 2389–2396

Paper VII **Highly insulating thermoplastic blends comprising a styrenic copolymer for direct-current power cable insulation**

Yingwei Ouyang, Amir Masoud Pourrahimi, Ida Östergren, Marcus Mellqvist, Jakob Ånevall, Azadeh Soroudi, Anja Lund, Xiangdong Xu, Thomas Gkourmpis, Per-Ola Hagstrand, Christian Müller

High Volt. 2022, 7(2), 251-259

Paper VIII **Highly insulating thermoplastic nanocomposites based on a polyolefin ternary blend for high-voltage direct current power cables**

Azadeh Soroudi, Yingwei Ouyang, Fritjof Nilsson, Ida Östergren, Xiangdong Xu, Zerui Li, Amir Masoud Pourrahimi, Mikael Hedenqvist, Thomas Gkourmpis, Per-Ola Hagstrand and Christian Müller

Nanoscale, 2022, 14, 7927

Table of Contents

1. Introduction

"Now is the time to scale up technologies and bring down costs to allow hydrogen to become widely used." Those are the words used by the International Energy Agency (IEA) in 2019 to describe the momentum of the hydrogen economy. The IEA states that it is time to take advantage of the full potential of hydrogen as a clean, secure, and cost-effective energy source.[1]

Hydrogen generates electricity or heat through a reaction with oxygen, which produces water as the only byproduct, which is preferable to fossil fuels with extensive emission of carbon monoxide and other air pollutants.[2, 3] This has led to increased attention to hydrogen as a potential clean, low emission, carbon-free energy source.[4] However, for the hydrogen economy to meet these expectations, the primary source of hydrogen must transition from coal and natural gas to renewable energy sources such as wind and solar power or biomass.[1, 5-10] One major benefit with hydrogen is that it can be used for storage of excess energy generated from solar cells or wind turbines on days when production is higher than the demand. Unused electricity can be utilized to split water into hydrogen that can be stored until the need for energy emerges (Figure 1.1).[2, 6, 9, 11]

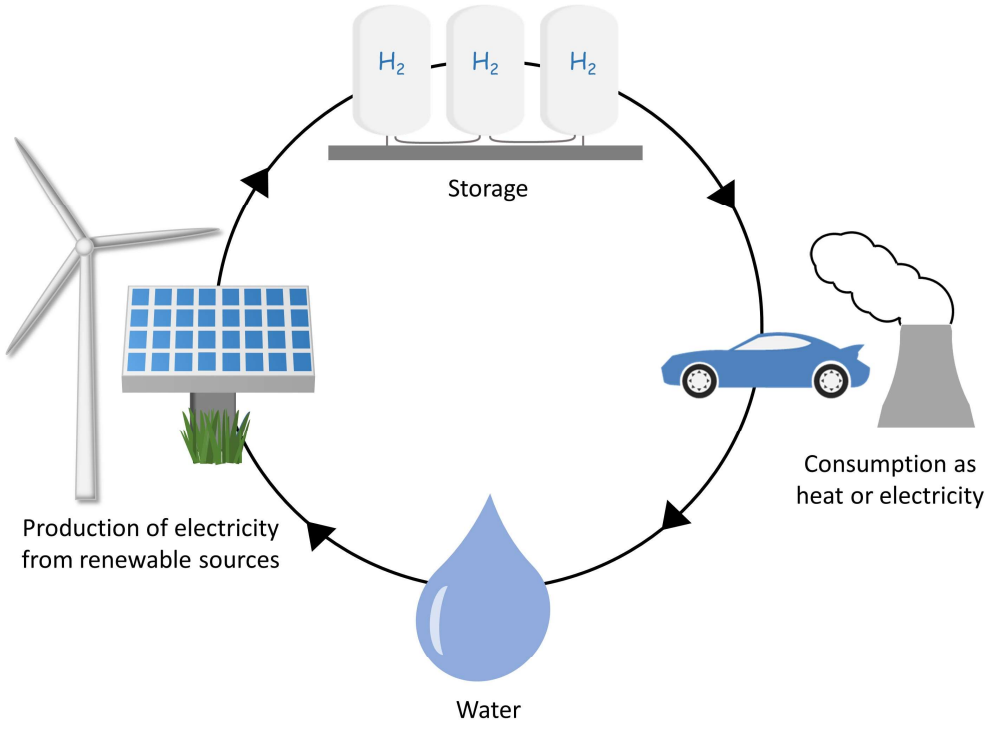

Figure 1.1. Illustration of the envisaged hydrogen economy.

There is significant potential versatility in hydrogen as a fuel, as it can be applied in a wide range of applications, from powering vehicles to heating or electricity generation. It has the potential to accelerate the reduction of carbon emissions in several sectors, including long-distance transportation, chemical synthesis and steel production.[1, 3, 12] However, it is crucial to handle hydrogen with caution since it has a low ignition energy and a high flammability in air, making it highly explosive. Additionally, it is prone to leaks because it is the smallest and lightest of all elements and is thus associated with a high diffusion rate.[13, 14] This makes it essential to have efficient, robust, and easy to use hydrogen sensors, to ensure safety throughout the entire life cycle from production to storage and end use.[12]

1.1 Hydrogen sensors

Hydrogen sensors are not only necessary to monitor the safety of hydrogen storage and production, but are also important for industrial process monitoring, e.g. during the synthesis of ammonia or the production of rocket fuels. Depending on the sensor application certain performance targets have been set by various industries and national governments (Figure 1.2).[13, 15-17]

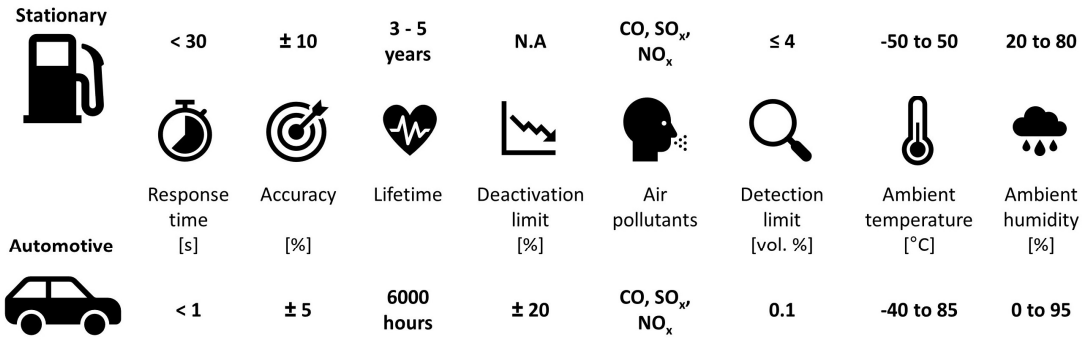

Figure 1.2. Performance targets and requirements for hydrogen safety sensors for stationary and automotive applications. Adapted from Ref.[17] Copyright American Chemical Society. 2020.

Currently, there are no hydrogen sensing technologies capable of reaching all these criteria. Achieving a rapid response time of 30 seconds for stationary applications and as low as 1 second for automotive applications, remains one of the most challenging requirements particularly when combined with a low detection limit. Another important requirement is the minimum lifetime of 5 years of the sensor, which is affected by temperature and the surrounding atmosphere including humidity and air pollutants. Air pollutants existing in urban air such as CO, SO_x and NO_x can poison the active sensor materials leading to deactivation of the sensor.[15, 17-19]

Hydrogen sensors work on the basis of interactions between H_2 and the sensing element, causing a change in temperature,[20] electrical[21-23]- or optical properties.[24-26] To avoid cross-sensitivity with other gases, palladium (Pd) or platinum (Pt) are the most common sensing elements due to their high selectivity for hydrogen in both catalytic reactions and absorption into the bulk, forming metal hydrides.[14, 27] Pd-based optical plasmonic sensors are promising due to their high selectivity towards hydrogen and because they facilitate ultrafast sensing at low hydrogen pressures.[28, 29] The optical signal enables a remote and spark-free readout due to its compatibility with optical fibres. Nonetheless, Pd-based plasmonic sensors comes with several challenges, including inherent hysteresis[30, 31] and susceptibility to poisoning from the CO found in urban air.[14, 15, 32]

1.2 Plasmonic hydrogen sensing

Localized surface plasmon resonance is a phenomenon occurring in noble metal nanoparticles where the free electron starts to oscillate when irradiated with incoming light (Figure 1.3a). At the resonance frequency of the oscillation the nanoparticles strongly absorbs and scatters light (Figure 1.3b).[33] Of the more readily available, single element nanoparticles, gold (Au) and silver (Ag) are the most widely investigated plasmonic materials due to their sharp plasmon resonances, whereas for palladium (Pd) and platinum (Pt), the resonance is dampened resulting in a broader extinction peak, with a lower total intensity.[34, 35] The wavelength and magnitude of the extinction depends on the shape, size, and composition of the metal nanoparticle as well as the surrounding local environment.[33, 36-39] This creates a possibility for a large diversity in the wavelengths of the scattered light, seen in the variety of colours present in plastic plasmonic materials containing Au spheres and rods, as well as Pd cubes (presented in Chapter 3 and 5).

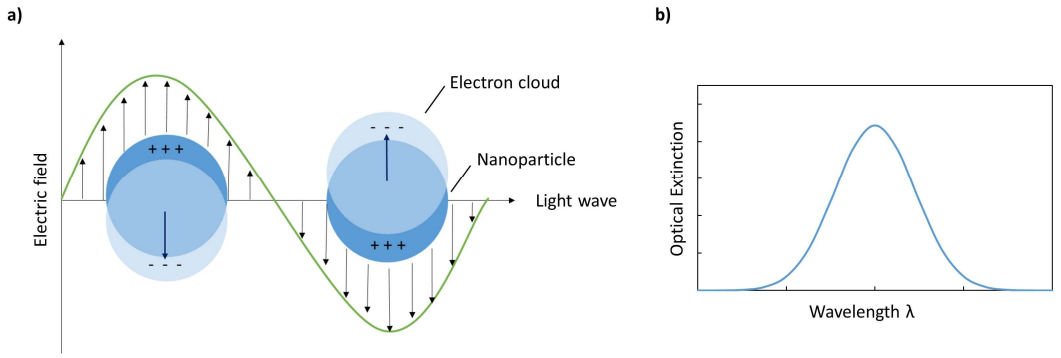

Figure 1.3. a) Schematic illustration of a) localized surface plasmon resonance of a metal nanoparticle. b) Optical extinction spectrum of a plasmonic nanoparticle.

The influence of the surrounding medium on the plasmon resonance is the basis for plasmonic sensors. Absorbed molecules on the surface of the plasmonic nanoparticles create a shift in the extinction peak, which is used as the sensor descriptor (Figure 1.4). Plasmonic sensors are utilized within a wide range of applications, with particular interest placed on biosensors[40, 41] for disease diagnosis,[39, 42, 43] biomolecule detection in wastewater[44-46], and gas sensors[47, 48] for monitoring air quality[49-51] or hydrogen detection.[17, 52, 53]

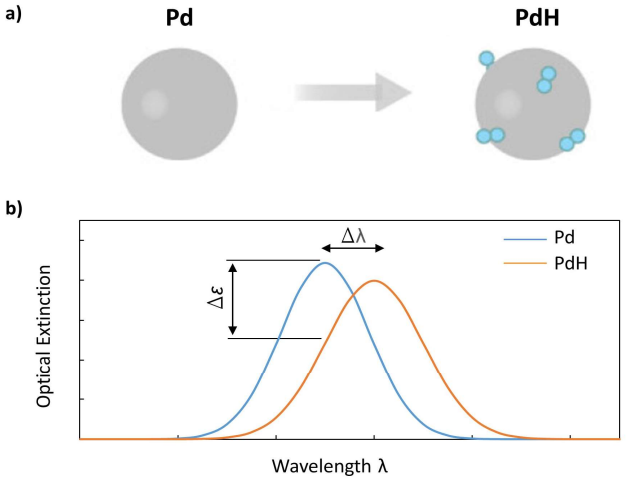

Figure 1.4. The concept of plasmonic hydrogen sensing a) The formation of PdH from Pd. b) The shift in the optical extinction upon PdH formation. Adapted in part from Ref.[63] Copyright American Chemical Society 2023.

Plasmonic hydrogen sensing is based on the ability of Pd crystals to adsorb hydrogen into the Pd lattice, resulting in the formation of PdH, which has a different plasmon resonance than pure Pd (Figure 1.4a).[54-56] This process is reversible and influenced by the ambient hydrogen pressure. The shift of the plasmon resonance extinction peak can be monitored in two ways: (1) by tracking the shift in the wavelength of the peak maximum, and (2) by observing the intensity change at a certain wavelength (Figure 1.4b). The magnitude of the shift in optical extinction is governed by the hydrogen pressure, making it a valuable tool for qualitatively analysing the hydrogen pressure.[52, 54, 57, 58]

Currently, state-of-the-art plasmonic sensors are Pd- or Pd-alloy based sensors fabricated with nanolithography and vacuum-based thin film material deposition.[17, 28, 32, 59, 60] These methods are time-consuming and limit the sensor design to flat 2D structures.[61, 62] To address these challenges we are in this work introducing the concept of plasmonic plastics consisting of plasmonic nanoparticles embedded in a polymer matrix. A paradigm shift towards polymer nanocomposites, includes large volumes of size and shape controlled colloidally synthesised nanoparticles together with common polymer processing techniques such as compounding, extrusion and 3D-printing.[63-65] This shift not only facilitates large-scale production, but also unlocks the potential to generate an infinite range of sensors shapes and designs. Incorporating Pd nanoparticles within a polymer matrix offers the dual advantage of enabling the formation of bulk structures and harnessing the polymer's potential to act as a molecular sieve and enhance the selectivity of the sensor.[66] In addition, the polymer matrix can protect Pd nanoparticles from deactivation,[28, 66] thus prolong the lifetime of the sensor.[67, 68]

2. Aim of this thesis

This thesis is focusing on answering the following research question: Is it possible to produce 3D-printable plasmonic polymer nanocomposites for hydrogen sensing? This research question has been divided into three separate aims:

1. Identification of polymers that would be suitable as a matrix material for a plasmonic hydrogen sensor while also exhibiting mechanical- and melt properties compatible for 3D-printing.
2. Development of a scalable processing route for plasmonic polymer nanocomposites that is compatible with a wide range of polymers and nanoparticles, to have the possibility of tailoring the material for specific applications.
3. Design of a plasmonic polymer nanocomposite, and a corresponding Pd based hydrogen sensor with a fast sensing response and a high selectivity towards hydrogen.

3. Material selection

The transition from 2D dimensional nanofabricated plasmonic sensors to sensor in 3D structures, produced with well-established processing techniques, could help facilitate facile production of plasmonic hydrogen sensors. I set out to investigate different polymers as matrix materials for 3D printable polymer nanoparticle composites to enable the production of plasmonic plastics. The goal was to establish how the selection of the polymer matrix affects the hydrogen sensing properties as well as the processability. In this chapter the first selection of various polymers is discussed together with an evaluation of the processability, optical properties, and gas diffusivity within the polymer.

3.1 Polymer Selection

In order to evaluate polymers that are suitable as the matrix material for 3D printable plasmonic polymer nanocomposites, in line with the first aim of this thesis, I started looking at the materials requirements from three different aspects: (1) Sensor requirements, (2) nanocomposite compatibility and processability, and (3) 3D printability.

For a polymer to be a good candidate from a sensing perspective it is of importance that it has a high H_2 permeability to generate a fast sensing response. At the same time the polymer must have a low permeability towards poisonous species such as carbon monoxide, CO. CO is present in low amounts in urban air and deactivates a Pd based sensor by inhibiting the dissociation of H_2. It is therefore crucial to have a barrier material that blocks out CO. The readout signal in a plasmonic hydrogen sensor is optical so the polymer needs to have a high light transparency. Depending on which application the sensor will be used for, e.g in fuel cells, properties such as heat deflection temperature (HDT), temperature resistance and chemical resistance need to be taken into consideration.

To be able to make a polymer nanocomposite through compounding and extrusion the polymer needs to be melt processable, meaning that it needs to have a suitable melt viscosity at temperatures lower than the onset of thermal degradation. The polymer must be compatible with the surfactants/stabilizer of the nanoparticles and the solvent used for the nanoparticle dispersion, in order to ensure a good distribution of the nanoparticles in the matrix.

To evaluate if a polymer is suitable for fused deposition modelling (FDM) 3D printing I examined: (1) the filament stiffness to ensure that the polymer can withstand the pressure put on the filament during feeding, (2) the melt viscosity, which must be sufficiently low so that the polymer melt easily can be extruded out of the nozzle but also high enough that the extruded strains maintain their shape and (3) the adhesion properties of the printed part to the build plate and between the printed layers.

I created a selection matrix (Table 3.1) to get an overview of possible polymers and their materials properties. The selection matrix was used as the basis for selecting polymers suitable for the fabrication of plasmonic plastics and their use as H_2 sensors. Polyethylene (PE) was added to the matrix for comparison since it is the most widely used commodity polymer.

Poly(methyl methacrylate) (PMMA), polyamide 6 (PA6), and poly(lactic acid) (PLA) were chosen for a proof-of-concept study with Au nanoparticles to show that plastic plasmonic materials can be produced. As seen in the selection matrix they are commonly used for melt processing and are likely to offer good compatibility with the nanoparticles due to the presence of polar groups (Figure 3.1). All three polymers are used for the preparation of filament for FDM printing,[69, 70] where PLA is the most widely used 3D printing material.[71] PMMA was also selected as a matrix for Pd nanoparticles because of its ability to function as a protective barrier towards CO in Pd based hydrogen sensors.[28, 66]

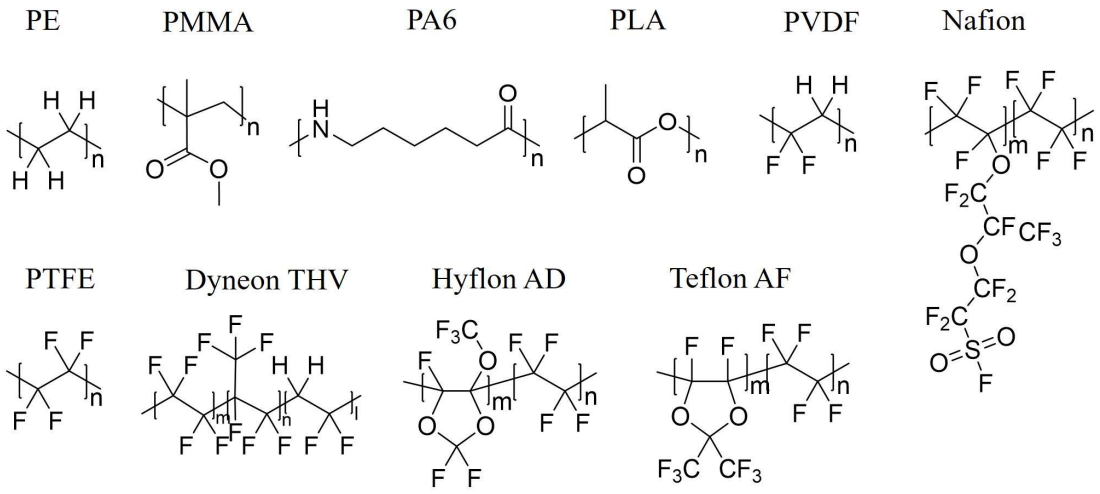

Figure 3.1. Polymer structures.

Fluoropolymers in general have good temperature stability and chemical resistance (see selection matrix Table 3.1). They are therefore attractive as a matrix material for hydrogen sensors. The most common fluoropolymer poly(tetrafluoroethylene) (PTFE) is unfortunately not a suitable choice because it cannot be melt processed due to its high melting temperature and high melt viscosity, which leads to thermal degradation before achieving proper melt flow.[72, 73] However there are a range of melt processable fluoropolymers such as semi-crystalline poly(vinylidene fluoride) (PVDF), Dyneon THV and a melt processable Nafion precursor (see Figure 3.1 for chemical structure). Nafion is of special interest since it is normally used as an ion exchange membrane in fuel cells and it is therefore already known to withstand these harsh conditions.[74, 75] Teflon AF and Hyflon AD are amorphous random copolymers with a high co-monomer content (see Figure 3.1 for chemical structure). The amorphous nature of these fluoropolymers give rise to optical clarity and a large fractional free volume that enables a high gas permeability,[76-78] making them an attractive alternative as the matrix material. Drawbacks with fluoropolymers are their poor adhesion properties and the risk of low compatibility with the nanoparticle dispersion.

Table 3.1. Selection matrix.

	PE[79, 80]	PMMA[79, 80]	PA6[79, 81, 82]	PLA[79, 83, 84]	PVDF[85]	PTFE[79, 86]	Teflon AF[86, 87]	Dyneon THV[86, 88]	Hyflon AF[86, 89]	Nafion[90]
Melt processable	✓	✓	✓	✓	✓	X	✓	✓	✓	✓
Temp. resistance	(✓)	(✓)	(✓)	X	✓	✓	✓	✓	(✓)	✓
HDT > 100 °C	X	(✓)	✓	X	✓	(✓)	✓	X	?	?
Fast H_2 diffusion	(✓)	(✓)	X	(✓)	X	X	✓	?	✓	?
Slow CO diffusion	✓	✓	?	?	✓	✓	X	?	X	?
Transparency	(✓)	✓	(✓)	✓	(✓)	(✓)	✓	✓	✓	✓
Compatibility with NPs	(✓)	✓	✓	✓	(✓)	X	?	?	?	?
Chemical resistance	(✓)	(✓)	X	X	✓	✓	✓	✓	✓	✓
FDM printability:										
Suitable viscosity	✓	✓	(✓)	✓	✓	X	✓	✓	✓	✓
Filament stiffness	✓	(✓)	✓	✓	✓	?	✓	✓	✓	(✓)
Adhesion	✓	✓	✓	✓	(✓)	X	X	X	X	X

3.2 Preparation of plasmonic polymer nanocomposites

There are two main approaches for preparing polymer nanocomposites from pre-polymerized polymer and pre-synthesized nanoparticles; solution mixing[91, 92] or melt compounding.[93, 94] Solution mixing entails dissolution of the polymer in a solvent to which a nanoparticle dispersion is added. The polymer:nanoparticle solution is mixed and later cast into a film. The main advantages are that homogenous distribution of nanoparticles can be achieved. In addition, several ink-printing methods can be used. The drawback is that a large amount of solvent is needed and that the structures are limited to thin films.[95] In the case of melt compounding the polymer and nanoparticles are mixed in a twin-screw extruder. This method is suitable for production at larger scale and for bulk structures. It is environmentally friendly due to the absence of solvent. The disadvantages are that the nanoparticles have a higher tendency to agglomerate and there is a risk for thermal degradation during processing depending on the polymer of choice.[95] I chose to work with melt compounding to have the advantage of being able to create a variety of shapes and sizes. With melt compounding I could also show that our material is suitable for the large-scale production needed for upscaling of plasmonic plastic hydrogen sensors.

3.2.1 Synthesis of nanoparticles

The nanoparticles used in the polymer nanocomposite need to be prepared before the compounding step. This allows for the possibility to syntheses a variety of compositions, shapes and sizes of the nanoparticle in order to tailor the properties of the polymer nanocomposite.[96, 97] In order to show the versatility of the plasmonic plastics concept, Au spheres of two different sizes and Au rods were synthesized by Alicja Stolas and Sarah Lerch for a proof-of-concept study. To apply the concept as a hydrogen sensor, Pd nanocubes were synthesized by two different routes. First, Alicja Stolas used colloidal batch synthesis to syntheses 23 nm large Pd cubes stabilized with hexadecyltrimethylammonium bromide (CTAB) (Figure 3.2).[98] At a later stage Robson Rosa da Silva produced Pd cubes with scalable continuous flow synthesis using poly(vinylpyrrolidone) (PVP) (Figure 3.2) as stabilizing agent.[99] This highlighted the possibility to continuously syntheses a large amount of Pd nanoparticles needed for upscaling of plasmonic plastics. To emphases the possibility of nanoparticle design with regards to composition Sarah Lerch also synthesised PdAu spheres stabilized with PVP.

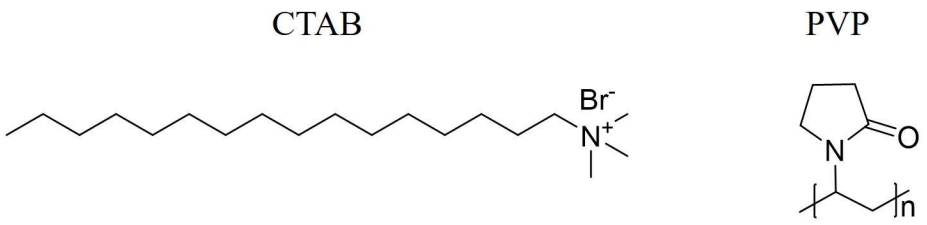

Figure 3.2. Chemical structures of the stabilizing agents.

The change from CTAB to PVP as a stabilizing agent was made because it has been reported that cationic surfactants such as CTAB decelerate the hydrogen adsorption onto Pd because of the strength of the halide-ion interaction with Pd.[100] PVP on the other hand experiences weaker interactions with the Pd surface and has an accelerating effect on the hydrogen absorption[100]. Nanoparticles stabilized with CTAB normally require water as dispersion medium, due to the ionic force between head group and dispersion medium. Water as the dispersion medium worked well together with polar polymers such as PMMA, PLA and PA6. In the case of fluoropolymers, Pd nanoparticles in a water dispersion did not mix well with the polymer powder because of poor wetting of the polymer (Figure 3.3a). This led to low incorporation of the Pd particles in the polymer matrix during compounding, as evidenced by the light color of the extruded filament (Figure 3.3c). Changing to PVP as the stabilizing agent, allow us to do a solvent exchange to the less polar solvent iso-propanol, which led to increased compatibility and sufficient mixing (Figure 3.3b) resulting in a composite with good incorporation of the nanoparticles, indicated by the dark brown color of the extruded filament (Figure 3.3c).

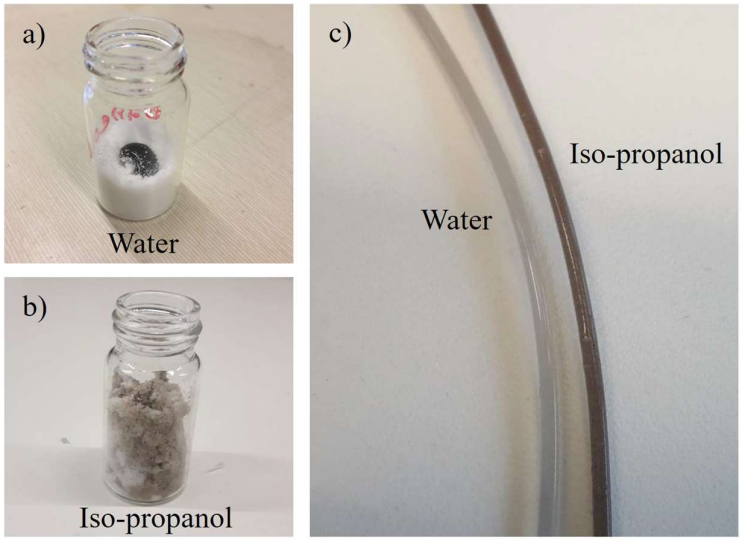

Figure 3.3. Dyneon THV nanocomposite a) Adding Pd nanocubes in water to Dyneon THV powder. b) Adding Pd nanocubes in iso-propanol to Dyneon THV powder. c) Extruded filaments of Dyneon THV:Pd from water dispersion and iso-propanol dispersion.

3.2.2 Compounding and extrusion of polymer nanocomposites

To address the second aim of this thesis, the development of a processing route for plasmonic polymer nanocomposites, I constructed a scheme containing four steps (Figure 3.4). First, the nanoparticle dispersion and polymer powder were mixed together, the mixture was then dried overnight, followed by melt compounding and extrusion into filaments suitable for 3D printing.

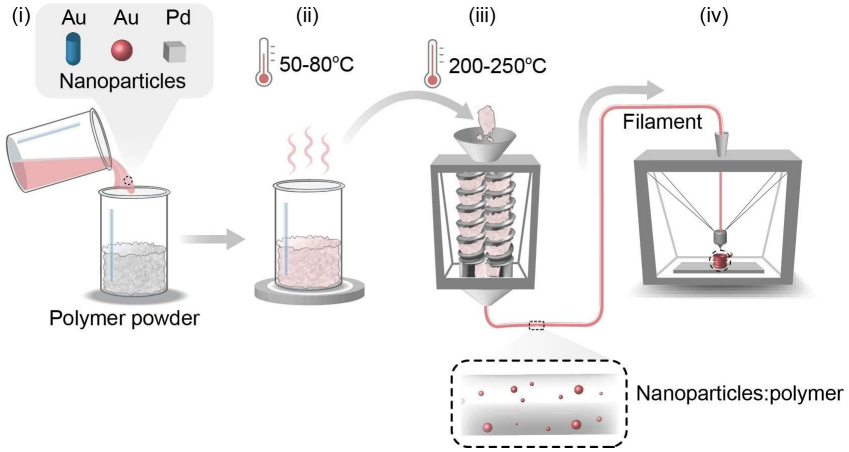

Figure 3.4. Processing scheme of plasmonic polymer nanocomposites i) mixing of nanoparticle dispersion with polymer powder. ii) Drying of polymer nanoparticle mixture. iii) compounding and extrusion of filament. iv) 3D-printing. Adapted from Ref. [63] Copyright American Chemical Society 2023.

As mentioned earlier PLA, PA6 and PMMA together with a variety of Au nanoparticles were selected for a proof-of-concept study. Table 3.2 shows the material combinations and processing settings for the study. The polymer:Au composites were compounded at different temperatures depending on their glass transition temperature (T_g) or where applicable melt temperature (T_m).

Table 3.2. Proof-of-concept study.

Polymer	PLA	PA	PMMA
Au NP shape	10 nm spheres	100 nm spheres	25x53 nm rods
NP content [wt. %]	0.0007-0.0256	0.0016-0.0083	0.0141-0.0491
$T_{prossesing}$ [°C]	200	220	200
Die size [mm]	1.75	1.75	1.0

The compounded polymer nanoparticle mixtures were extruded into filaments with a diameter of approximately 1.75 mm, the diameter size needed for feeding of the filament to a Massportal Pharaoh XD 3D printer. To obtain the right filament diameter it is necessary to choose the right die size (Table 3.2). The main factor affecting the choice of the die is the degree of die swelling by the polymer melt as it exits the die. Extrudate swelling is an elastic stress relaxation phenomenon, that occurs when a polymer melt is stretched while entering a small capillary and then relaxes when exiting the capillary.[101] Chain relaxation gives rise to a cross section larger than the cross section of the capillary exit. The Deborah number (*De*) describes the ratio between the time it takes for a material to adjust to the applied stress and the characteristic time scale of the process where the relaxation time is defined as the ratio between melt viscosity, η, and the elastic modulus, E.

$$De = \frac{Relaxation\ time\ of\ the\ material}{timescale\ of\ the\ process} \qquad \text{(eq. 3.1)}$$

$$Relaxation\ time = \frac{\eta}{E} \qquad \text{(eq. 3.2)}$$

If the relaxation time of the material is longer than the timescale of the process, the material will still be experiencing stress at the exit, stress relaxation and therefore die swelling will occur. At a fixed shear rate, the die swell can be minimized by decreasing the viscosity of the polymer melt, this can be done by increasing the temperature or by choosing a polymer grade with a lower molecular weight.

I compensated the die swell by choosing a die with a smaller diameter so that the right filament size was obtained taking die swelling into account. For example, PMMA exhibits a high degree of die swell and needs a small die with a diameter of 1 mm to obtain a filament with a diameter of 1.75 mm. The degree of die swell in PMMA is reduced by the addition of nanoparticles because the movement of the molecular chains are blocked by the solid nanoparticles and the elastic recovery is hindered.[102] The addition of nanoparticles also improves the printability of PMMA composites, by blocking the chain relaxation, thereby decreasing the relaxation time. The shrinkage upon solidification is reduced, hence less warping occurs (see Chapter 5).[103]

The extruded filaments were then either melt pressed with a hot press into 500 µm thick plates (Figure 3.5a-c) or 3D-printed into a variety of shapes (see Chapter 4). The PA6:Au composites had to low melt viscosity and melt strength during compounding to be able to form a filament upon extrusion (Figure 3.6) and could therefore not be used for 3D printing. They also suffered

from slight thermal degradation in each processing step, seen by the appearance of a slightly yellow color (Figure 3.5b). Hence PA6 was not a suitable choice for 3D-printable plasmonic plastics.

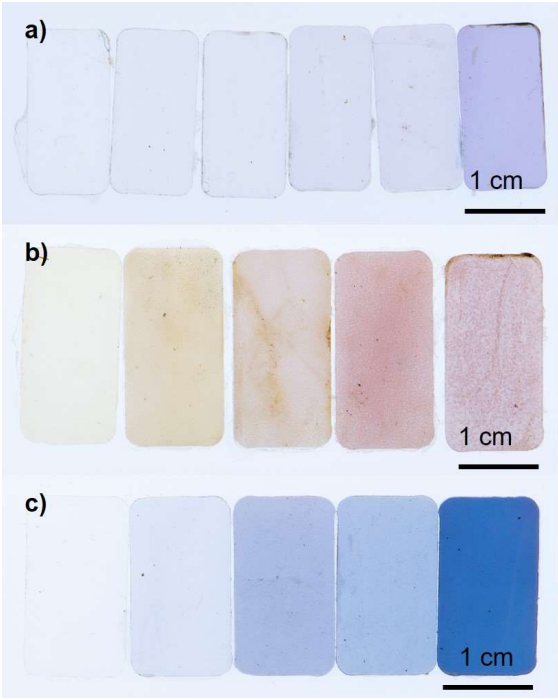

Figure 3.5. Photos of 500 μm melt pressed plates of a) Neat PLA and PLA:Au composites containing 0.0007-0.0256 wt. % of 10 nm Au spheres. b) Neat PA6 andPA6:Au composites containing 0.0016-0.0083 wt. % of 100 nm Au spheres c) neat PMMA and PMMA:Au composite containing 0.0141-0.0491 wt. % of 25x52 nm Au rods. Adapted in part from Ref.[63] Copyright American Chemical Society 2023.

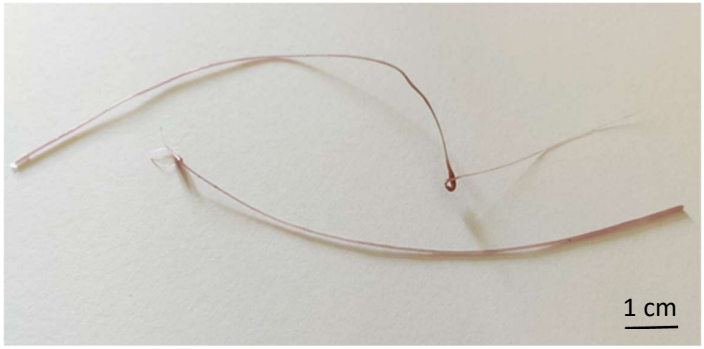

Figure 3.6. Photo of extruded PA6:Au composite.

Transmission electron microscopy (TEM) images of PLA:Au and PMMA:Au, obtained by Alicja Stolas, reveal that the incorporated Au nanoparticles have preserved their shape and size through the compounding and extrusion steps (Figure 3.7). Elemental analysis of the PLA:Au, PA6:Au and PMMA:Au revealed that the Au concentration in the composites scales linearly with the Au nanoparticle concentration in the added dispersion (Figure 3.8). This indicates a robust processing route that allows to tailor the selection of polymer and nanoparticles as well as the particle content in the composite.

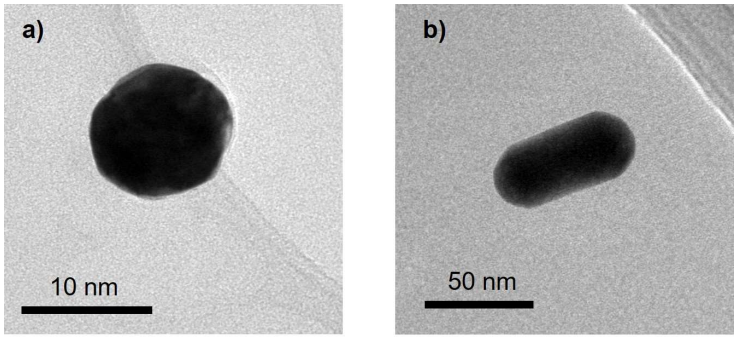

Figure 3.7. TEM images of a) Au sphere incorporated in PLA and b) Au rod incorporated in PMMA, Images obtained by Alicja Stolas. Adapted from Ref.[63] Copyright American Chemical Society 2023.

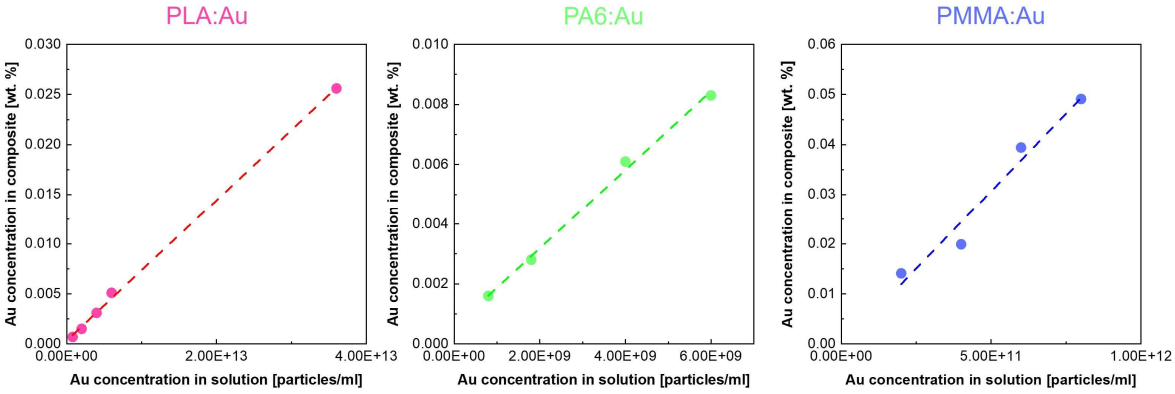

Figure 3.8. Au concentration in the final composite against Au concentration in the added dispersion.

To address the third aim of this thesis, the development of a plasmonic polymer nanocomposite for hydrogen sensing, I also prepared a series of nanocomposites containing Pd cubes. As mentioned earlier in this chapter, PMMA was selected as a matrix polymer because of its ability to protect Pd against CO poisoning, together with a range of fluoropolymers including PVDF, Dyneon THV, Teflon AF and Hyflon AD. Nafion, which was an interesting candidate, could not be grind into a powder. Hence, no mixing with the Pd dispersion was possible and no composite could be produced.The selected polymers and Pd cubes were mixed, compounded, and extruded using the same scheme described for Au composites (Figure 3.4). One composite with a set Pd content was made with PVDF, Dyneon THV and Hyflon AD, whilst for PMMA and Teflon AF a series of composites with a range of Pd contents were made (Table 3.3 and Figure 3. 9).

Table 3.3. Processing of Pd nanocomposites.

Polymer	PMMA	PVDF	Dyneon THV	Teflon AF	Hyflon AF
Pd NP shape	10 nm cubes	10 nm cubes	10 nm cubes	10 nm cubes	10 nm cubes
NP content [wt. %]	0.01-0.16	0.015	0.011	0.011-0.08	0.012
$T_{prossesing}$ [°C]	200	200	240	250	220
Die size [mm]	1.0	1.75	1.5	1.5	1.5

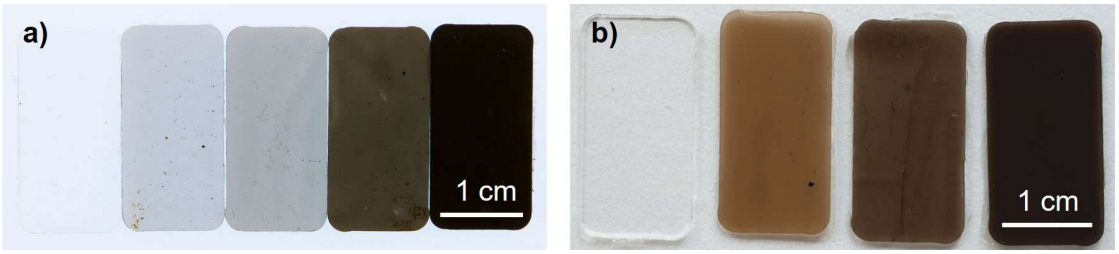

Figure 3.9. Photos of 500 µm melt pressed plates a) Neat PMMA and PMMA:Pd composites containing 0.01-0.16 wt. % of 10 nm Pd cubes and b) Neat Teflon AF and Teflon AF:Pd composites containing 0.011-0.08 wt. % of 10 nm Pd cubes. Adapted from Ref.[64] Copyright American Chemical Society 2021 and from Ref.[65] Copyright American Chemical Society 2020

The processing temperature needed for compounding of the different polymer:Pd composites (Table 3.3) affected the shape of the Pd nanocubes due to the reconstruction of the Pd nanoparticles at high temperatures.[99] TEM images, obtained by Alicja Stolas, reveal that for PMMA:Pd processed in the lower temperature range, the Pd nanocubes retains their cubic shape but with slightly rounded edges (Figure 3.10b). For Teflon AF:Pd the higher processing temperature of 250 °C had a stronger influence on the Pd nanocubes, as evidenced by TEM imaged obtained by Sarah Lerch and Robson da Silva, which reveal that the particles have lost their initial cubic shape in favor of the more entropically stable spherical shape (Figure 3.10d).

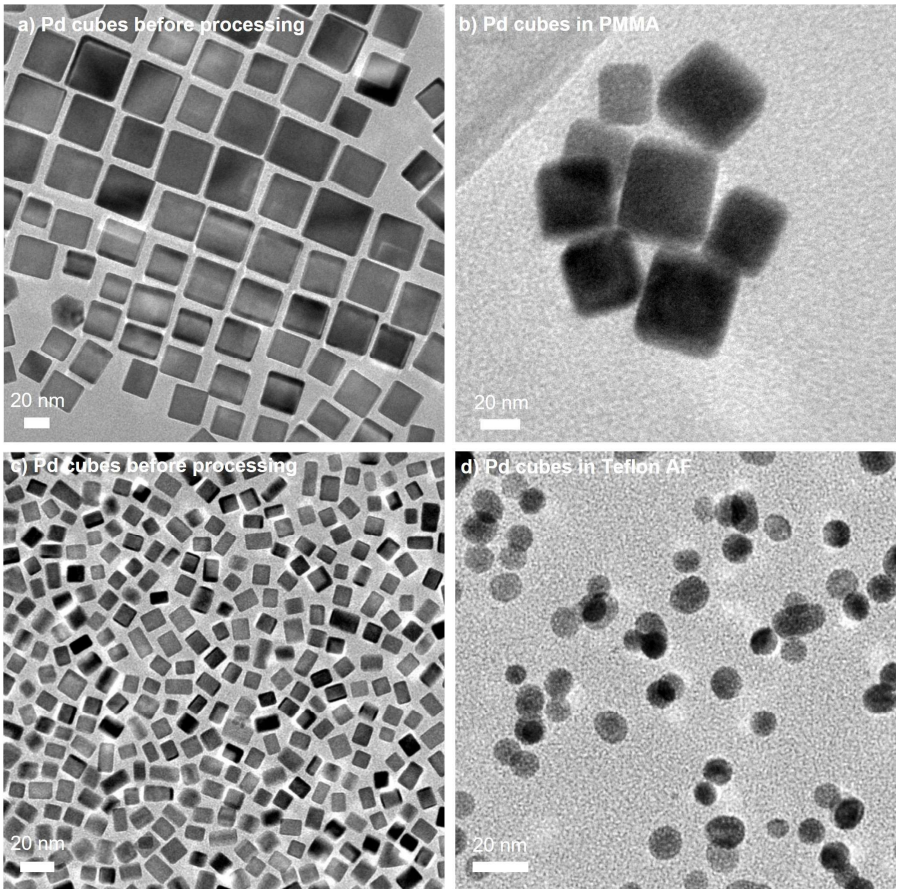

Figure 3.10. TEM images of a) as synthesized Pd cubes before incorporation in PMMA b) Pd cubes after incorporation in PMMA c) as synthesized Pd cubes before incorporation in Teflon AF. d) Pd cubes after incorporation in Teflon AF. TEM Images obtained by Alicja Stolas, Robson Rosa da Silva and Sarah Lerch. Adapted in part from Ref.[65] Copyright American Chemical Society 2021.

Elemental analysis of the PMMA:Pd and Teflon AF:Pd composite series of (Paper I and II) also revealed a linear trend between the added amount of Pd particles and the Pd concentration in the final composite. These results indicate that the processing route developed for Au composites could be transferred to Pd composites, whose use as hydrogen sensors will be discussed in Chapter 5.

3.3 Transmittance of visible light

The plasmonic peak for most nanoparticles and especially nanoparticles relevant for plasmonic plastics is situated in the visible region of the Ultraviolet-Visible (UVVis) absorption spectra (Paper IV, Figure S4).[104] The read out from a plasmonic hydrogen sensor consists of a shift in wavelength for the position of the plasmonic peak. It is of high importance that the polymer matrix does not absorb or strongly scatter light in the same region as the plasmonic peak. To evaluate the transparency, UVVis absorbance spectra were recorded for 100 μm thick films of the selected neat polymers and the corresponding nanocomposites.

All neat polymers exhibit a low absorbance in the visible region (Figure 3.11). The lowest absorbance is observed for the two amorphous fluoropolymers, Teflon AF and Hyflon AD, but also PMMA and PLA exhibits low absorbance in the visible region. The overall extinction in the UVVis spectra increase for the semi-crystalline polymers, Dyneon THV and PVDF, indicating a lower transparency. This is due to an increase in scattering at the boundary between the amorphous and crystalline regions and by large spherulites.[105] PVDF, which has the highest degree of crystallinity,[85] therefore has the highest overall value of absorbance and scattering in the UVVis spectra. With regards to the optical properties, Teflon AF and Hyflon AD are the best choice for a plasmonic plastics matrix material.

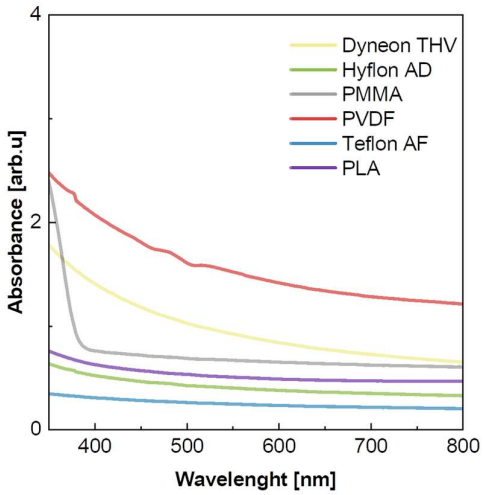

Figure 3.11. UVVis spectra of 100 µm thick films of the neat polymers.

To ensure that the plasmonic resonance of the embedded nanoparticles is unaffected by compounding and extrusion of the nanocomposite, UVVis spectra were recorded for the PLA:Au nanospheres, PMMA:Au nanorods, and PMMA:Pd nanocubes composites (Figure 3.12). For PLA:Au nanosphere composites one distinct peak is found around 570 nm, which corresponds to the plasmonic peak of Au spheres.[106] Two peaks are visible around 550 nm and 650 nm for PMMA:Au nanorods, corresponding to the short and long rod axis respectively.[107, 108] For PMMA:Pd nanocubes there is a broad peak ranging from 400-700nm, which matches the peak expected for Pd nanocubes.[36, 64] All nanocomposites exhibit a plasmonic resonance that matches the peak position of the respective type of nanoparticle in colloidal dispersion, indicating that the plasmonic resonance of the particles is preserved in the polymer matrix. Each nanoparticle contributes to the total light absorption, as evidenced by the increase in the total absorbance with high Pd content (Figure 3.12), in agreement with Beer−Lambert law.[109, 110] This shows that plasmonic polymer nanocomposites can be produced through melt processing and that the intensity and position of the plasmonic peak can be altered with nanoparticle shape and concentration.

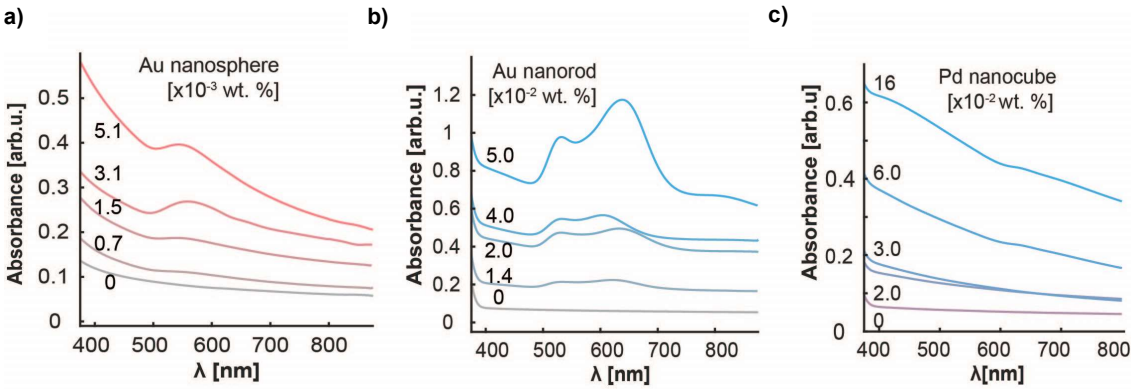

Figure 3.12. UV/VIs spectra 500 µm thick films of a) PLA:Au nanospheres composites, b) PMMA:Au nanorods composites, 2023and c) PMMA:Pd nanocubes composites. Adapted from Ref.[64] Copyright American Chemical Society 2020 and Ref.[63] Copyright American Chemical Society 2023.

3.4 Hydrogen diffusion

Fast diffusion of hydrogen through the polymer matrix enables the gas to quickly reach the Pd nanoparticles, which will ultimately result in a sensor with a rapid response.

The transport of a gas through a polymer film consists of five steps (Figure 3.13):[111]

1) Diffusion of the gas to the surface of the polymer film, 2) Adsorption of the gas by the polymer film at the interface, 3) Diffusion through the bulk of the film, which is the most time-consuming step and therefore becomes rate limiting, 4) Desorption of the gas from the polymer film and 5) Diffusion of the gas away from the polymer film.

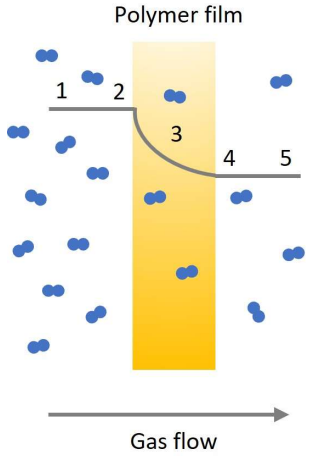

Figure 3.13. Schematic of the steps for gas transport through a polymer film.

Gas transport through the bulk of a polymer film is usually described with a solution-diffusion model, where there are two separate contributions to the permeability, P,

$$P = D * S \qquad \text{eq. 3.3}$$

where the solubility, S, is the thermodynamic contribution defined as the amount of gas molecules dissolved in the polymer film and the diffusivity, D, is the kinetic contribution defined as the mobility rate of the gas molecules inside the polymer film. To evaluate these three parameters, time- lag experiments[112] were conducted in collaboration with Matteo Minelli and Giacomo Foli at University of Bologna.

Time-lag experiments were conducted according to ASTM D1434-82, the standard test method for determining the gas permeability characteristics of plastic films and sheetings[113]. The hydrogen gas was allowed to diffuse from an upstream chamber that had a constant pressure of approximately 1.2-1.5 bar, though a polymer film with a 2.2 cm^2 area to a downstream chamber, which at the beginning of the experiment was made vacuum. The penetrant flux was obtained from the increased pressure in the downstream chamber[76, 112].

By plotting the amount of gas that has passed though the polymer film against time, the gas permeability, P, can be derived from the slope at steady state (Figure 3.14). The permeability is calculated according to:

$$P = J_{ss}\frac{l}{\Delta p} = \left(\frac{dp_d}{t}\right)_{t\to+\infty}\frac{V_d}{R\,T\,A}\frac{l}{\Delta p} \qquad \text{eq. 3.4}$$

where J_{ss} is the penetrant molar flux per unit area at steady state, Δp, the pressure difference, p_d the downstream pressure, V_d the calibrated volume of the downstream chamber and A the membrane area. Diffusion kinetics are evaluated from the time-lag at the beginning of the measurement, the diffusivity D, can thus be calculated according to:[114]

$$D = \frac{l^2}{6\,\theta_L} \qquad \text{eq. 3.5}$$

where θ_L (time-lag value), is determined as the intercept on the time axis (x-axis) of tangent from the slope steady state (Figure 3.14).[76, 115]

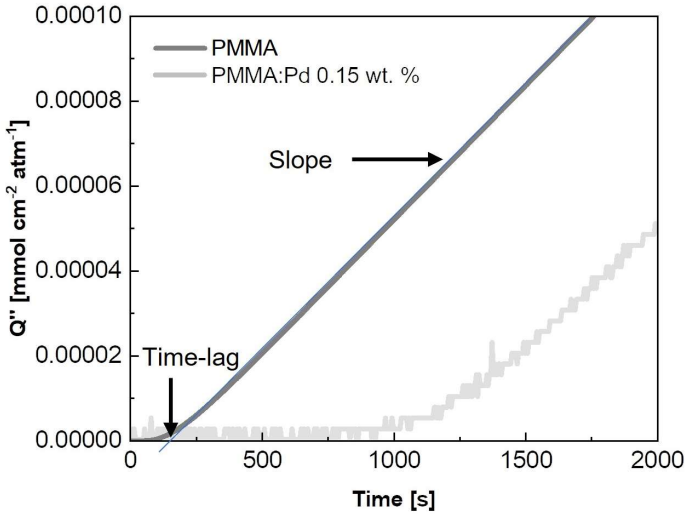

Figure 3.14. Time-lag measurement of neat PMMA and PMMA:Pd with 0.15 wt. % of Pd. Data obtained by Giacomo Foli. Adapted from Ref.[64] Copyright American Chemical Society 2020.

First, we investigated the gas transport properties of neat polymers films. Since the rate-limiting step for the gas transport through a polymer film is diffusion through the bulk of the film (Figure 3.12, step 3), hence the parameter that has the main influence of the hydrogen transport to the Pd nanoparticles is the diffusivity. There is a wide spread in diffusivity values ranging from low values of $5.9 \cdot 10^{-8}$ cm^2 s^{-1} for PVDF to high values of $2.3 \cdot 10^{-5}$ cm^2 s^{-1} for Teflon AF (Table 3.4). The low diffusivity for PVDF originates from the high degree of crystallinity, where the presence of crystals results in a more tortuous path of diffusion. The diffusivity is lower for semi-crystalline compared to amorphous polymers since the absence of crystals enables hydrogen to move more direct. Comparing the amorphous polymers with each other, the main influence on diffusivity comes from the fractional free volume (FFV) i.e. the amount of free space where the hydrogen molecules can move.[76] The FFV is affected by the size of the side groups, Teflon AF and Hyflon AD have large bulky side groups (Figure 3.1) compared with PMMA, which gives rise to a larger FFV and hence diffusivity.[116] From a hydrogen diffusion perspective, Teflon AF and Hyflon AD are the two most promising candidates for a plasmonic hydrogen sensor.

Table 3.4. H_2 permeability, solubility, and diffusivity.

	Permeability [barrer]	Solubility $[cm^3 \cdot (cm^2)^{-1}]$	Diffusivity $[cm^2 \cdot s^{-1}]$
Teflon AF	745	0.24	$2.32 \cdot 10^{-5}$
Hyflon AD	160	0.19	$6.32 \cdot 10^{-6}$
Dyneon THV	6.49	0.04	$1.38 \cdot 10^{-6}$
PMMA	4.18	0.05	$6.58 \cdot 10^{-7}$
PVDF	0.45	0.058	$5.87 \cdot 10^{-8}$

Secondly, we examined the effects of adding Pd nanoparticles to the polymer matrix. The addition of Pd nanoparticles to PMMA drastically increases the time-lag (Figure 3.14). This change is due to the reaction of hydrogen with Pd resulting in the formation of PdH. Initially, all the adsorbed hydrogen in the PMMA film is consumed by Pd nanoparticles. Once all the Pd nanoparticles are saturated with hydrogen, the excess hydrogen diffuses through the PMMA film and desorbs into the downstream chamber. The permeability of PMMA:Pd compared to PMMA is unaffected by the addition of Pd nanoparticles, as evidenced by a comparable slope in the steady state region. Once all the Pd nanoparticles are saturated with hydrogen, the hydrogen diffusion is no longer hindered by the Pd nanoparticles, and the permeability is therefore constant.

For Teflon AF and Teflon AF:Pd composite the effect on the time-lag by adding Pd nanoparticles is not as pronounced as for PMMA:Pd (Paper II, Figure 3a). The increase in time lag is noticeable but small and the permeability is unaffected. The lesser effect on Teflon AF:Pd composites can be explained by the higher permeability of hydrogen. The overall amount of hydrogen present in the Teflon AF film is higher and therefore the Pd nanoparticles saturate quickly. The small effect on the diffusivity by adding Pd nanoparticle to Teflon AF highlights the suitability of Teflon AF as the matrix material.

4. Up-scaling of PMMA:Au composite

For new polymeric materials, the transition from lab-scale, typically a few grams, to industrial scale, sometimes on the order of hundreds of kilograms, can be challenging. Therefore, the second aim of this thesis is to develop a scalable processing route for plasmonic polymer composites. To demonstrate the potential scalability for plastic plasmonic composites and highlight the possibility of large scale production, Robson Rosa da Silva, Amir Masoud Pourrahimi, Anja Lund and I produced 2 kg of PMMA:Au nanospheres composite. While this production level is still far away from an industrial scale (approximately 1 million tons of polymer nanocomposites are manufactured each year[117]), it highlights the potential for plasmonic plastics to transition from the lab scale to the kilogram scale and, hopefully, beyond.

Many polymer processing techniques are readily compatible with large scale production. Melt processing techniques such as extrusion and injection molding, developed during the 19th century, were applied to synthetic polymers such as polyethylene during the 1940s.[101] The compounding process where additives such as pigments, reinforcement agents or nanoparticles are added to a neat polymer, utilizes a co- or counter rotating twin screw extruder that blends polymer and the various additives to achieve an adequate dispersion.[101]

The main challenge for up-scaling of plasmonic plastics lies with the nanoparticle synthesis. The majority of size- or shape-specific nanoparticles are still produced through batch synthesis, allowing for close control of the parameters that influence the size, shape and crystal structure.[118] Issues with poor heat- and mass transfer limits batch synthesis to small scale, generally less than 1 L of solution per synthesis. To upscale nanoparticle synthesis, Robson da Silva developed a flow synthesis method that produces shape- and size-controlled citrate capped Au nanospheres in water.[63] This method enables a fast and continuous production of the large amounts of Au nanospheres needed for upscaling (Figure 4.1b).

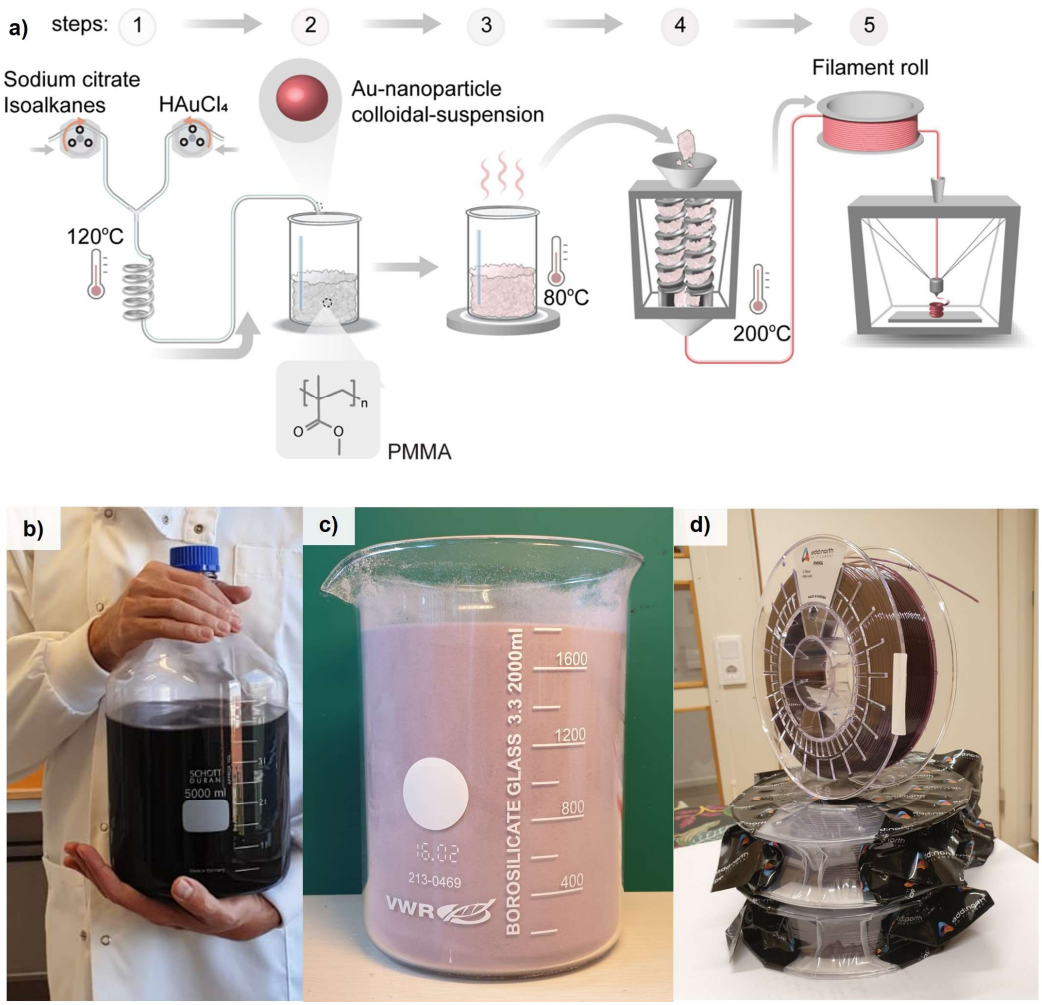

Figure 4.1 Upscaling of plasmonic plastics. a) Processing scheme b) Large scale flow synthesized Au nanospheres in water dispersion. c) PMMA and Au nanosphere powder mixture. d) Three rolls of PMMA:Au nanospheres 3D-printing filament. Adapted from Ref.[63] Copyright American Chemical Society 2023.

A nanocomposite production methodology was developed by Anja Lund, Amir Masoud Pourrahimi and myself, to facilitate the production of plasmonic plastics on the kilogram-scale (Figure 4.1a). The Au nanosphere dispersion (Figure 4.1b) was mixed with 2 kg of PMMA powder, forming a slurry that was stirred while heating to remove a large amount of the water and then further dried under vacuum. The obtained polymer:Au nanosphere mixture (Figure 4.1c) was compounded, extruded and cut into granulates at RISE in Mölndal and then further extruded into a 400 m long filament (Figure 4.1d), at the production facility of Add:North, to

be used as the feedstock for 3D-printing (Chapter 5). The produced filament has an Au content of 0.01 wt. %.

The produced granulates and filament, together with the 3D-printed structures (Chapter 5, Figure 5.2), demonstrate the scalability, versatility, and processability of plasmonic plastics. This indicates that this class of material is suitable for further upscaling.

To be able to enable further up-scaling of plastic plasmonic materials additional enhancements are required, since the leap to industrial levels are still prominent:

(1) The development of a continuous flow synthesis methodology of nanoparticles where the nanoparticle concentration is increased to reduce the amount of water that needs to be evaporated during drying. Or the addition of a concentration step.
(2) The use of large-scale industrial mixers for homogenous and efficient mixing.
(3) The use of a continuous conveyor oven for efficient drying.

With regard to compounding and extrusion, both the compounding step (granulates) and the 3D printing filament production step, the type of infrastructure that was used at RISE and Add:North is sufficient for handling larger quantities.

5. 3D printing of plasmonic plastics

3D-printing, which can also be called additive manufacturing, is a bottom-up manufacturing technique where thin layers of material are placed on top of each other to build up a structure[119]. The first 3D-printer for polymers, introduced in the 1980s, was a stereolithography (SLA) machine, which uses UV or visible light to cure photopolymers within a resin[120]. Since then, several different methods have been developed including selective laser sintering (SLS) and powder bed fusion (PBF), which uses a laser or electron beam to melt a polymer powder and fuse the powder particles together.

Today, fused deposition modeling (FDM) is the most widely used 3D-printing technique for polymers. FDM uses a solid polymer filament as the feedstock, which is melted immediately prior to the print nozzle and a motor pushes the remaining solid filament so that it acts as a piston that pushes the melted polymer out. During this process, the printer head moves over the build plate and deposits the molten polymer. After deposition, the polymer cools down and solidifies. A new layer is then printed on top of the previous layer, until the structure is complete.[121]

The general scheme to produce a part through 3D-printing starts with a computer aided design (CAD) model of the part, that depicts the external 3D-geometry of the part.[119] A 3D-printing slicing software transforms the CAD model by slicing it into thin cross-sectional layers. The slicing software also provides the printer settings, such as temperature, printing speed, layer height, extrusion multiplier etc. There is also the possibility to add additional structures that will help facilitate the printing such as brim, raft, or support structures. The slicing software creates a geometric code (.g-code file) that is transferred to the 3D-printer. The 3D-printer reads the defined settings from the slicing software and proceeds to deposit the molten material onto a printing surface. The printer builds up the part, layer by layer according to the slicing of the CAD model.

At first 3D-printing was mainly used for 3D visualization models and prototypes but as the methods and material options developed, a wide range of fields have identified additional use.[119, 122] 3D-printing is more time consuming compared to conventional manufacturing techniques, but it offers the possibility to produce materials in a large variety of shapes and designs. For example, 3D-printing gives access to complex designs that are difficult to achieve with conventional manufacturing, like parts with high porosity or an all-in-one-build of parts

that otherwise would need to be assembled.[123] The final product can also be custom-made for a specific purpose such as prosthetics and high-end sports equipment. Another possibility is on-site production to minimize lead time and to reduce the quantity of manufactured parts to precisely match the required amount. Small quantities of an item can be produced compared to injection moulding where large scales are needed for it to be worth the time and cost to produce the moulds. The produced waste is significantly reduced with 3D-printing compared to milling or carving where a lot of material is cut away to produce the item.

One of the challenges for FDM printing is the limited diversity of commercially available material.[120] To expand the scope of the FDM technology the available materials need to go beyond neat polymers such as PLA, acrylonitrile butadiene styrene (ABS) based compounds and high impact polystyrene (HIPS) and transition to functional materials to make use of FDM for more complex applications. One way of adding functionality to the 3D-printable filament is to make polymer nanocomposites, where the properties of the material can be modified at the nanoscale[124]. Among available options one can find filament that has incorporate either carbon black or graphene for electrical conductivity,[125, 126] or copper oxide nanoparticles for antimicrobial properties.[127]

To go beyond the state of the art and utilize plasmonic plastics for FDM printing is not only intriguing for aesthetic reasons,[128] but it also holds significant potential for introducing sensing functionality.[129] This new approach can broaden the range of materials available for FDM printing and contribute to the field of sensing, where 3D printing has emerged as a promising concept.[130]

5.1 3D printing of PLA- and PMMA Au composites

PLA is one of the most widely used polymers in FDM printing because it is easy to print, has a low cost and is environmentally friendly.[71] Therefore, PLA:Au composites were chosen as a proof-of-concept material, to demonstrate that plastic plasmonic nanocomposites can be 3D-printed. Neat PLA and PLA:Au composites with 0.0015 and 0.0256 wt. % of Au nanospheres were used to 3D-print the Swedish Foundation of Strategic Research (SSF) Logo (Figure 5.1). The 3D-printing of PLA was straightforward and uncomplicated, and standard recommendations for printing settings could be used (Table 5.1).[71] Incorporating Au nanospheres into PLA did not influence its printability and the same processing parameters used for pure PLA could be applied without any adjustments.

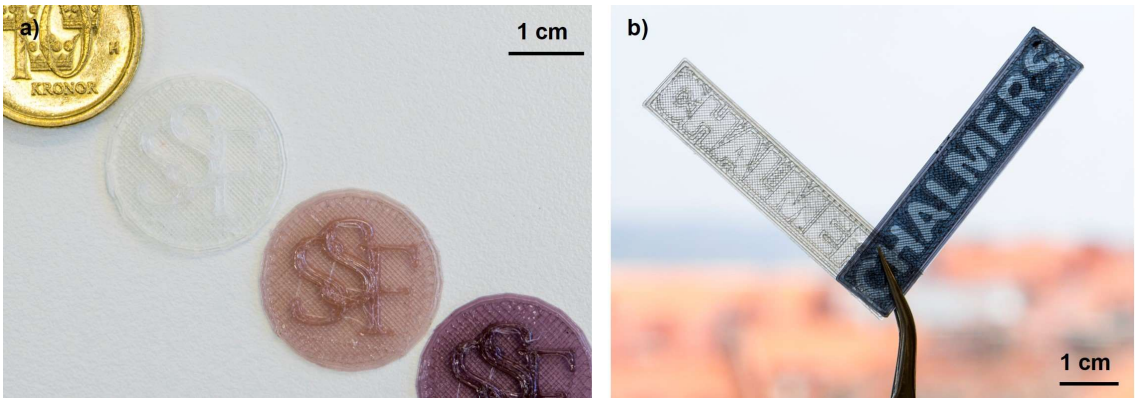

Figure 5.1. Photo of 3D-printed structures a) SSF logo 3D-printed with neat PLA and PLA:Au composites with 0.0015 and 0.0256 wt. % of Au nanospheres and b) Chalmers logo 3D-printed with neat PMMA and PMMA:Au composite with 0.02 wt. % of Au nanorods. Photos by Petri Murto. Adapted from Ref.[63] Copyright American Chemical Society 2023.

Table 5.1. 3D-printing settings for PLA:Au nanospheres and PMMA:Au nanorods. $T_{printing}$ is the temperature of the polymer melt during printing and $T_{build\ plate}$ is the temperature of the 3D printers heated build plate.

	PLA:Au nanospheres	PMMA:Au nanorods
$T_{printing}$ [°C]	210	210
$T_{build\ plate}$ [°C]	60	60
Nozzle size [mm]	0.4	0.4
Layer thickness [mm]	0.2	0.2
Printing speed [mm/min]	2000	1000
Other	-	Brim with 8 outlines of PLA

To continue the assessment of the printability of plastic plasmonic nanocomposites, neat PMMA and PMMA:Au with 0.02 wt. % of Au nanorods were used to 3D-print the Chalmers logo (Figure 5.1) using the printing settings specified in Table 5.1. To achieve a good printability of PMMA, some additional aspects were taken under consideration: (1) PMMA shrinks upon cooling which can cause warping, a phenomenon where, at first, the print adheres well to the build plate but later during the printing process, the bottom layers start to curl at the

edges until the warping is so severe that the part detaches from the build plate,[131] (2) die swell at the nozzle exit similar to die swell during filament extrusion (see Chapter 3).

To reduce the warping, a brim with eight outlines in PLA was printed to increase the bed adhesion and to hold down the edges of the PMMA print. The die swell of PMMA during printing was reduced by selecting a lower printing speed, which increased the time scale of the process (see Deborah number, Chapter 3). The addition of Au nanorods to PMMA increased the printability by reducing the orientation of polymer chains, which led to a lower degree of shrinkage of the polymer.[103]

5.1.1 3D-printing with upscaled PMMA:Au filament

To demonstrate that plasmonic plastics could be used to 3D-print larger and more complex structures, I 3D-printed miniature versions of the Vinga lighthouse and beacon (Figure 5.2) with the PMMA:Au nanosphere filament, from the plasmonic plastic upscaling (see Chapter 4). The PMMA:Au nanosphere filament was of high quality with excellent printability, which enabled stable printing over a long period of time without the risk of overheating. The printed lighthouse and beacon were designed with 1 mm small features, which were printed with high accuracy showing the great quality and printability of the PMMA:Au filament.

Figure 5.2. Photo of 16 and 20 cm tall miniature versions of the Vinga beacon and lighthouse 3D-printed with PMMA:Au nanosphere filament. Photography by Malin Arnesson/Chalmers.

In order to address the printing challenges associated with PMMA, a slightly different approach was used compared to PMMA loaded with Au nanorods. To eliminate the need of using PLA for the brim but still preserve sufficient adhesion to the build plate, the build plate temperature was set to 110 °C for the first printed layer (see Table 5.2). The build plate temperature was

then decreased to 60 °C for the rest of the print to allow for solidification of PMMA. Printing these larger parts also require a higher printing speed in order to maintain a reasonable time frame. To increase the printing speed while avoiding die swell, the printing temperature was increased to 260 °C (See Table 5.2). The increased printing temperature lowered the melt viscosity of PMMA:Au nanosphere composite and thereby the relaxation time of the melt, which compensated for the shortened time scale of the process (See Deborah number, Chapter 3). For the top scepter of the lighthouse and beacon, the printing speed was reduced to 500 mm/min to allow the previous layer to solidify before the next layer was placed on top.

Table 5.2. Printing settings for PMMA:Au nanospheres.

Polymer	PMMA:Au nanospheres
$T_{printing}$ [°C]	260
$T_{build\ plate}$ [°C]	60 (110 for first layer)
Nozzle size [mm]	0.4
Layer thickness [mm]	0.2
Printing speed [mm/min]	3600 (500 for top scepter)
Other	Brim with 10 outlines of PMMA

The various structures printed using PLA:Au and PMMA:Au filaments confirm the creation of a 3D-printable polymer nanocomposite containing plasmonic nanoparticles. Thanks to versatility of FDM 3D-printing, it is possible to generate a wide variety of shapes and sizes of the plasmonic plastics.

5.2 3D printing of PMMA- and Teflon AF Pd composites

To address the third aim of this thesis, the design of plasmonic polymer nanocomposites for Pd based hydrogen sensing, I 3D-printed sensor caps that fit on an SMA 905 fiber optic connector for a "plug and play" style sensor (Figure 5.3c,d). For PMMA:Pd with 0.02 wt. % of Pd, the print settings for PMMA:Au nanospheres were used (Table 5.3) and a sensor cap consisting solely of PMMA:Pd was printed (Figure 5.3a,c).

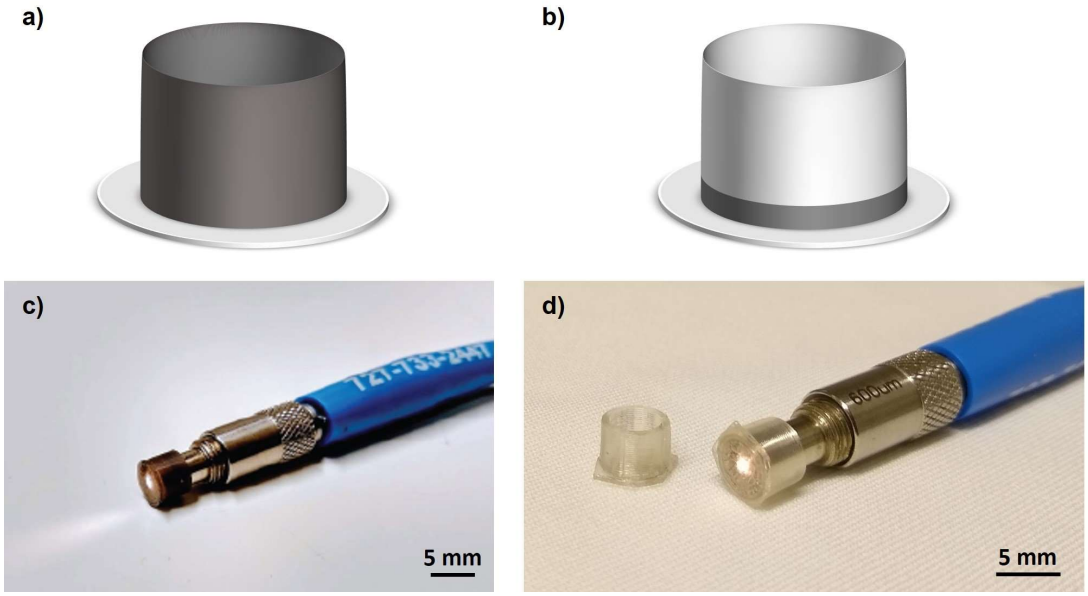

Figure 5.3. Illustration of sensor cap a) PMMA:Pd and b) Teflon AF:Pd (grey highlights the parts consisting of composite material containing Pd; white part consists of PLA), c) Photo of 3D-printed sensor cap made with PMMA:Pd. d) Photo of 3D-printed sensor cap made with Teflon AF:Pd and PLA. Adapted from Ref.[64] Copyright American Chemical Society 2020 and from Ref.[65] Copyright American Chemical Society 2021.

Due to the perfluorinated structure of Teflon AF, the Teflon AF:Pd composite suffered from poor layer-to-layer adhesion as well as insufficient adhesion to the build plate. To address this issue and optimize the use of Teflon AF:Pd composite, the cap design was altered so that only the bottom of the sensor cap, is made of Teflon AF:Pd (Figure 5.3b). The side wall of the cap and the brim consist of PLA. For Teflon AF:Pd composite with 0.023 wt. % of Pd, the cap was printed with similar settings as for PMMA:Pd but with an increased printing temperature due to the higher T_g of Teflon AF compared to PMMA (Table 5.3).

Table 5.3. 3D-printing settings for PMMA:Pd and Teflon AF:Pd.

	PMMA:Pd nanocubes	Teflon AF:Pd nanocubes
$T_{printing}$ [°C]	210	260
$T_{build\ plate}$ [°C]	60	60
Nozzle size [mm]	0.4	0.4
Layer thickness [mm]	0.2	0.2
Printing speed [mm/min]	1000	1000
Other	Brim with 8 outlines of PLA	Brim with 8 outlines of PLA

The 3D-printed sensor caps containing PMMA:Pd and Teflon AF:Pd could be used as prototype sensors for the detection of hydrogen (see Chapter 6). Evidently, 3D printing of plasmonic plastics for hydrogen sensing is feasible provided that the matrix polymer is carefully selected.

6. Sensing properties of polymer:Pd composites

To evaluate how the design of the plasmonic nanocomposite sensor influences the sensing performance in accordance with the third aim of this thesis, I prepared samples of the different polymer:Pd nanocomposites for which Iwan Darmadi performed sensing experiments. The investigated design parameters were (1) the polymer matrix, (2) the Pd content in the composite and (3) the sensor thickness. Two different experimental set ups were used for H_2 sensing experiments, as described in Paper I. During H_2 sensing the polymer:Pd sensors are exposed to H_2 under vacuum or in a controlled atmosphere (Figure 6.1a). The formation of PdH_x from Pd causes a shift in the plasmonic resonance of the nanoparticles.[31, 52, 132] The sensor response was recorded as self-referenced optical extinction spectra, $\bar{\varepsilon}$, defined as the difference in optical extinction prior to H_2 exposure, $\varepsilon_{Pd}(\lambda, t)$, (Figure 6.1b grey line) and after optical extinction upon H_2 exposure, $\varepsilon_{PdH_x}(\lambda, t)$, (Figure 6.1b green line) normalized by $\varepsilon_{Pd}(\lambda, t)$.

$$\bar{\varepsilon}(\lambda) = 1 - \frac{\varepsilon_{PdH_x}(\lambda,t)}{\varepsilon_{Pd}(\lambda,t)} \qquad (6.1)$$

Self-referenced optical extinction spectra of the hydrogenated composite feature a maximum and minimum $\bar{\varepsilon}(\lambda_{max}, t)$ and $\bar{\varepsilon}(\lambda_{min}, t)$ (Figure 6.1b). The difference in extinction, at λ_{max} and λ_{min} in the optical extinction spectra is used as the readout parameter, according to eq. 6.2.

$$\Delta\bar{\varepsilon}(t) = \bar{\varepsilon}(\lambda_{max}, t) - \bar{\varepsilon}(\lambda_{min}, t) \qquad (6.2)$$

The change in $\Delta\bar{\varepsilon}$ over time during a stepwise increase in H_2 pressure, followed by a stepwise decrease, is recorded to determine the response and recovery time of the hydrogen sensor. The response time, $t_{50,resp}$, is defined as the time it takes to reach 50 % of the total sensor response, for a stepwise increase of the H_2 pressure. This is highlighted in Figure 6.1c, where a stepwise increase (green) and decrease (orange) of H_2 is shown, the dashed line indicates 50 % of the signal. The recovery time, $t_{50,rec}$, is defined in the same way i.e., the time it takes to reach 50 % of the total sensor response for a stepwise decrease in H_2 pressure.

The maximum response of the hydrogen sensor, $\Delta\bar{\varepsilon}_{max}$, is an indicator of the sensitivity of the sensor. A large sensor response allows to distinguish small changes in the H_2 concentration. The maximum sensor response is defined as the difference between $\Delta\bar{\varepsilon}$ of fully hydrogenated Pd and non-hydrogenated Pd (eq. 6.3 and Figure 6.1c).

$$\Delta\bar{\varepsilon}_{max} = \Delta\bar{\varepsilon}_{PdHx} - \Delta\bar{\varepsilon}_{Pd} \qquad (6.3)$$

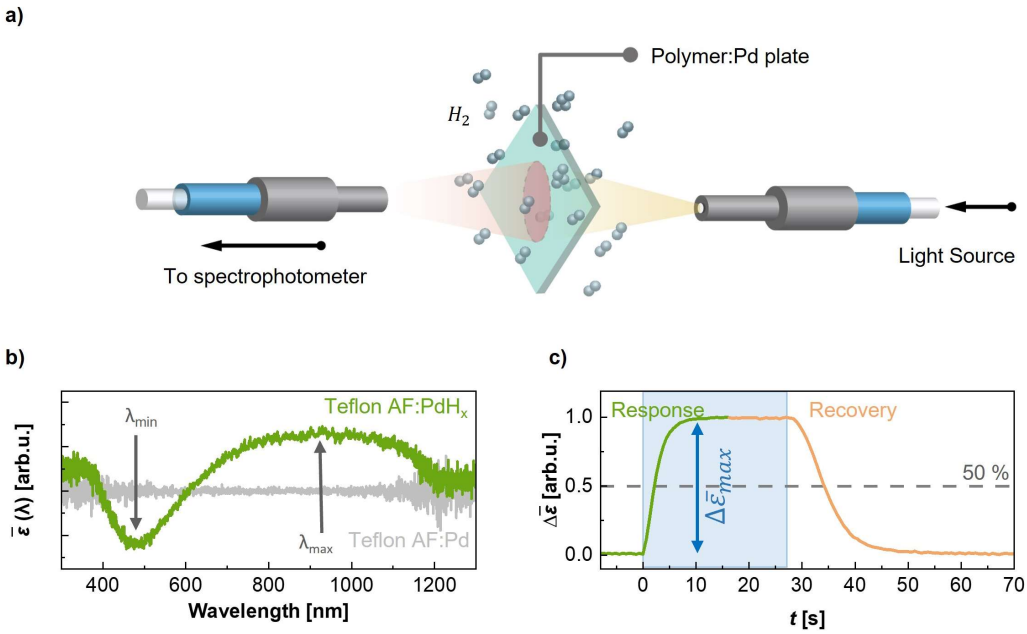

Figure 6.1. Plasmonic hydrogen sensing. a) Schematic of optical H_2 detection via optical extinction measurements through a melt pressed nanocomposite plate. b) Self-referenced extinction spectra of Teflon AF:Pd coated with 250 nm of PMMA exposed to 0 mbar H_2 (grey) and 100 mbar H_2 (green). c) Normalized $\Delta\bar{\varepsilon}$ of Teflon AF:Pd coated with 250 nm of PMMA, upon a stepwise increase (green) and decrease (orange) in H_2 pressure from 0 to 100 mbar, blue region marks the presence of 100 H_2 mbar.

6.1 PMMA:Pd nanocomposites

Hydrogen sensors used in urban air are exposed to air pollutants such as CO, NO_x, and SO_x. If these poisonous species reach the Pd nanoparticle they will block the ability for H_2 to dissociate on Pd and therefore deactivate the sensor. It has previously been shown that PMMA can act as a molecular sieve and therefore prevent the diffusion of poisonous species though the sensor.[28, 66] Hence, we evaluated the ability of PMMA to act as a protective barrier by studying the sensing kinetics of the PMMA:Pd composites, to understand how the selection of PMMA as a matrix material influences the sensing performance.

To investigate the possibility to influence the response time of the sensor via the PMMA:Pd composition, I prepared a series of samples comprising different amounts of Pd, ranging from 0.02 to 0.16 wt. %. The PMMA:Pd composites were melt pressed into 250 µm thick plates. The PMMA:Pd plates were exposed to a stepwise increase from 0 to 750 mbar of H_2, and $\Delta\bar{\varepsilon}$ was monitored (Figure 6.2a). The response time, $t_{50,resp}$, increases linearly with Pd content of the composite (Figure 6.2b). With more Pd particles present, the time it takes for all Pd particles to be saturated with H_2 increases, hence the response time increases. This is in line with the increase in time lag during permeability measurements for PMMA:Pd compared to neat PMMA (Chapter 3, Figure 3.14). A similar trend is seen for $\Delta\bar{\varepsilon}_{max}$ (Figure 6.2c) which increases with a higher particle content. Every single Pd particle contributes to the sensor response, therefore with more particles present the overall signal increases. This is also seen in the UVVis spectra (Chapter 3, Figure 3.12c), where a higher Pd content in the composite results in a higher light absorbance. Both, a short response time and a large $\Delta\bar{\varepsilon}_{max}$ are desirable sensor properties, which requires a compromise of the chosen Pd content in the sensor so that a "good-enough" level of both properties is obtained.

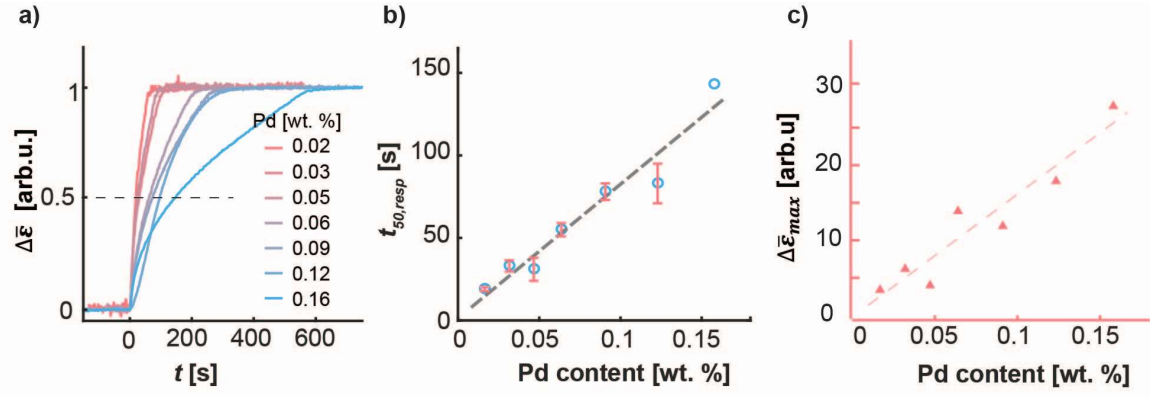

Figure 6.2. Hydrogen sensing of 250 µm thick PMMA:Pd plates with increasing Pd content. a) $\Delta\bar{\varepsilon}$ of PMMA:Pd composite upon a stepwise increase of H_2 pressure from 0 to 750 mbar. b) Response time, $t_{50,resp}$, vs. Pd content in the composites (error bars denote the standard deviation of three measurements. c) $\Delta\bar{\varepsilon}_{max}$ vs. Pd content in the composites. Data recorded by Iwan Darmadi. Adapted from Ref.[64] Copyright American Chemical Society 2020.

I prepared a series of PMMA:Pd composites with 0.02 wt. % of Pd melt pressed into plates with a range of thicknesses varying from 100 to 800 µm in order to study the impact of the geometry of the sensor. The impact of the thickness of the sensor on the sensing kinetics was evaluated thorugh a serie of expermients that involved a stepwise increase of the H_2 pressure from 0 to 750 mbar (Paper I, Figure 4c). The response time, $t_{50,resp}$, of the sensor increases quadratically with the sensor thickness (Figure 6.3a) due to two different effects. First, the diffusion time of H_2 through the sensor plate increases with inceased plate thickness, which has previously been reported[59]. Secondly, an increased sensor thickness leads to an incresed volume of the sensor hence a higher total amount of Pd particles is present in the sensor. The higher amount of particles increases the time it takes for all Pd particles to be saturated as seen in the Pd concentration study (Figure 6.2). The $\Delta\bar{\varepsilon}_{max}$ increases linearly with the sensor thickness (Figure 6.3b), due to the increase of the amount of Pd particles in the sensor, where each particle contributes to the $\Delta\bar{\varepsilon}_{max}$. The results show the necessity to consider the shape and size of the produced sensor, where a thinner sensor design provides a fast sensor reponse while a thicker sensor design enables a sensor with higher sensitivity.

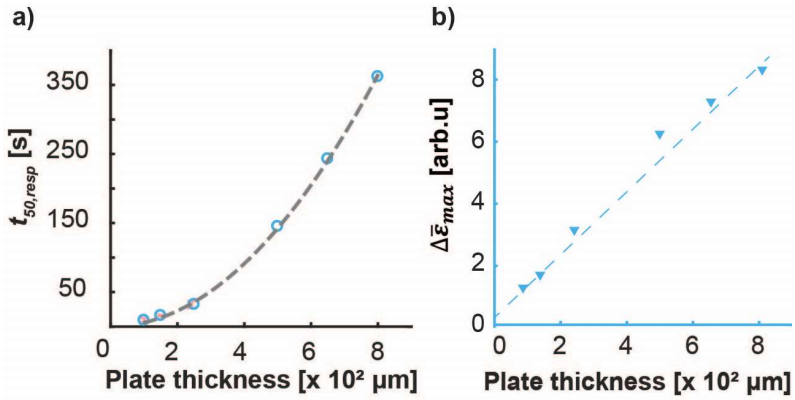

Figure 6.3. Hydrogen sensing of PMMA:Pd plates with different thicknesses. a) Response time, t_{50}, vs plate thickness. b) $\Delta\bar{\varepsilon}_{max}$ vs plate thickness. Data recorded by Iwan Darmadi. Adapted from Ref.[64] Copyright American Chemical Society 2020.

To evaluate the protective properties of PMMA against CO, I prepared a sample of the PMMA:Pd composite with 0.03 wt. % Pd that was melt pressed into a 100 µm thick plate. The sensor was exposed to five cycles of synthetic air containing 10 % H_2, secondly five cycles of synthetic air containing 0.5 % CO and finally five cycles of synthetic air containing 10 % H_2

and 0.5 % CO (Figure 6.4a). Bare Pd nanoparticles on a silica substrate and neat PMMA were used as a reference. When only H_2 is present both PMMA:Pd and bare Pd particles have a clear sensing response. With the addition of CO to the synthetic air the bare Pd particles deactivated quickly resulting in the loss of most of the sensing signal. PMMA:Pd, on the other hand, retained its sensitivity in the presence of CO. This confirms the selective molecular sieving function of PMMA, where H_2 diffuses through the PMMA plate but CO is blocked. PMMA is therefore a good choice of matrix material for the purpose of creating a protective barrier around the Pd particles.

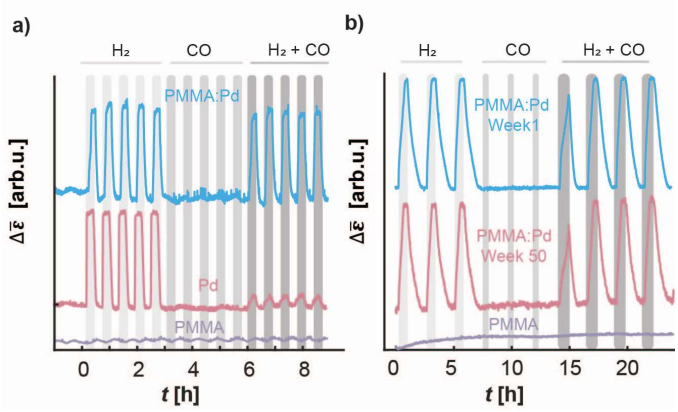

Figure 6.4. Hydrogen sensing in synthetic air with and without CO present. for a) melt pressed PMMA:Pd plate, with bare Pd particles and a neat PMMA plate as reference. b) 3D-printed PMMA:Pd sensor cap, 1 week after printing and 50 weeks after printing, with a 3D-printed sensor cap of neat PMMA as a reference. Data recorded by Iwan Darmadi. Adapted from Ref. [64] Copyright American Chemical Society 2020.

A sensor cap of PMMA:Pd with 0.2 wt. % Pd content with a 200 µm layer thickness was 3D-printed (see Chapter 5, Figure 5.3) to demonstrate the processability and ability to produce a variety of shapes of PMMA:Pd as well as the sensor compatibility with commercial optical fibers. The sensor cap was exposed to three cycles of synthetic air containing 10 % H_2, secondly three cycles of synthetic air containing 0.5 % CO and finally four cycles of synthetic air containing 10 % H_2 and 0.5 % CO (Figure 6.4b). The 3D-printed sensor cap exhibits a stable H_2 sensing response with and without the presence of CO, highlighting the flexibility of the sensor geometry that can be achieved with plasmonic polymer nanocomposites. The experiment was repeated after 50 weeks to evaluate the long-term stability of the sensor. The sensor response of the 3D-printed cap is unaffected after 50 weeks of aging in air, showing that PMMA

protects the Pd particles both from ambient air and CO poisoning, resulting in a sensor with a long shelf life.

6.2 Assessment of the choice of polymer matrix

To investigate the possibility to influence the response time of the sensor via the selection of the matrix polymer, I prepared composites with different polymers: PMMA, PVDF, Dyneon THV, Hyflon AD, Teflon AF. Composites containing around 0.01 wt. % of Pd were melt pressed into 100 µm thick plates. Sensing kinetics evaluation was performed through both a stepwise increase and decrease of the H_2 pressure between 0 to 100 mbar (Figure 6.5a). Teflon AF:Pd and Hyflon AD:Pd have an immediate response to the presence of H_2 with a response time, $t_{50,resp}$, of 3 s (Table 6.1). PMMA:Pd and Dyneon THV:Pd are slower with $t_{50,resp}$ = 51 s and 82 s, respectively. The trend is the same but is notably more pronounced when it comes to the recovery time, $t_{50,rec}$, (Figure 6.5b and Table 6.1). The sensing response for PVDF:Pd was too slow to achieve a saturated signal within 2 hours, so the experiment was terminated.

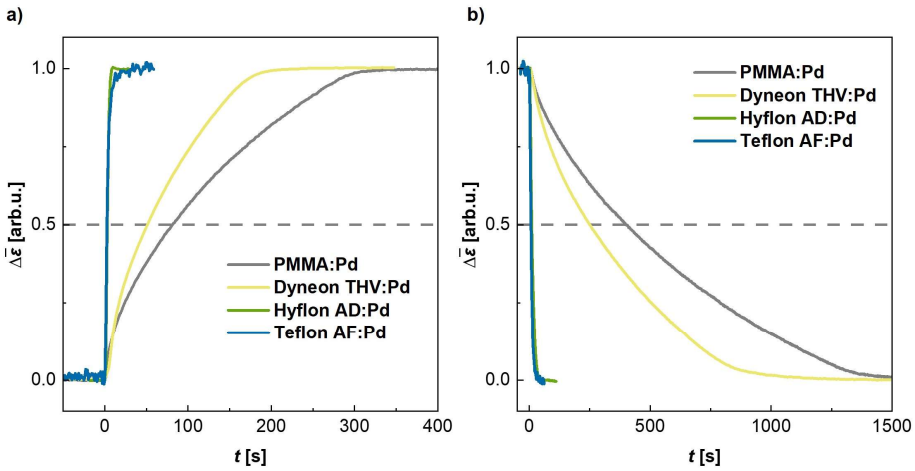

Figure 6.5. Hydrogen sensing of 100 µm thick polymer:Pd plates. a) $\Delta\bar{\varepsilon}$ upon a stepwise increase of H_2 pressure from 0 to 100 mbar. b) $\Delta\bar{\varepsilon}$ upon a stepwise decrease of H_2 pressure from 100 to 0 mbar. Dash grey line denotes 50% of the total signal. Data recorded by Iwan Darmadi.

The response times, $t_{50,resp}$, of the sensors correlate with the diffusivity coefficient of the polymer (Table 3.4, Chapter 3), where Teflon AF had the highest diffusivity followed by Hyflon AD. PMMA and Dyneon THV have a one order of magnitude lower diffusivity compared to Teflon AF and Hyflon AD, which correlates with the slower response and recovery

for Dyneon THV:Pd and PMMA:Pd. The slow diffusion of H_2 through the PMMA:Pd and Dyneon THV:Pd composites means that it takes longer time for H_2 reaches the Pd particles, resulting in a slow sensing response. This is particularly evident in the case of PVDF, which exhibits the lowest diffusivity, resulting in the inability of PVDF:Pd to display a saturated signal. This clearly highlights the importance of selecting a matrix polymer with high hydrogen diffusivity to facilitate a hydrogen sensor with fast response time.

Table 6.1. Response and recovery time for a stepwise increase, 0 to 100 mbar, and decrease, 100 to = mbar, of hydrogen pressure.

	Response time, $t_{50,resp}$ [s]	Recovery time, $t_{50,rec}$ [s]
Teflon AF:Pd	3	7
Hyflon AD:Pd	3	10
Dyneon THV:Pd	51	247
PMMA:Pd	82	400
PVDF:Pd	Not saturated	Not saturated

6.3. Teflon AF:Pd composites

Teflon AF has a remarkably high gas diffusivity compared to other polymers due to its large FFV. This generated a fast H_2 sensing response, within seconds, for the Teflon AF:Pd composites. To assess how the high hydrogen diffusivity of Teflon AF impacts sensor design, I created a set of samples that consist of Teflon AF:Pd composites with 0.02 wt. % of Pd. The composites were melt pressed into plates with various thicknesses ranging from 50 to 650 μm. Sensing kinetics evaluation during a stepwise increase from 0 to 100 mbar (Paper II, Figure 4c and S7,) shows that all the thicknesses for Teflon:Pd composites have a considerably shorter response time compared to PMMA:Pd, thanks to the high H_2 diffusion rate. A response time of 2-3 s is reached for the thinner sensors with a thickness of 50-250 μm. A thicker plats results in a longer response time, that scales quadratically with the sensor thickness (Paper II, Figure 4d) in the same way as for PMMA:Pd. The $\Delta\bar{\varepsilon}_{max}$ scales linearly with the sensor thickness (Paper II, Figure 4e), also seen in PMMA:Pd. The choice of Teflon AF as the matrix polymer has enabled a fast sensor, where the response time and optical contrast can be tuned by altering the sensor thickness.

To investigate how the high gas diffusivity of Teflon AF influences the sensor design with regards to Pd content, I prepared a series of 100 µm thick Teflon AF:Pd composites with a Pd content ranging from 0.01 to 0.08 wt. %. These samples were evaluated through measurements of the hydrogen sensing kinetics (Figure 6.6a-b). Remarkably, the Teflon:Pd composites exhibit a fast response, around 2-3 s, independent of the Pd content. The high FFV of Teflon AF enables fast diffusion of H_2, which generates a high concentration of H_2 in the bulk of the sensor and allows all the Pd particles to be saturated simultaneously. This is consistent with time lag measurements, which showed that the introduction of Pd to Teflon AF had only a minor impact on the time-lag. (Paper II, Figure 3a). The characteristic diffusion time of hydrogen through a 100 µm thick Teflon AF plate is 0.8s, which is less than the hydrogen absorption time reported for bare Pd nanoparticles (Paper I, Figure S3c). The sensor response time is no longer limited by hydrogen diffusion though the bulk of the polymer. The $\Delta\bar{\varepsilon}_{max}$ of Teflon AF:Pd composites increases linearly with higher content of Pd in the composite (Figure 6.6c), similar to PMMA:Pd (Figure 6.2c).

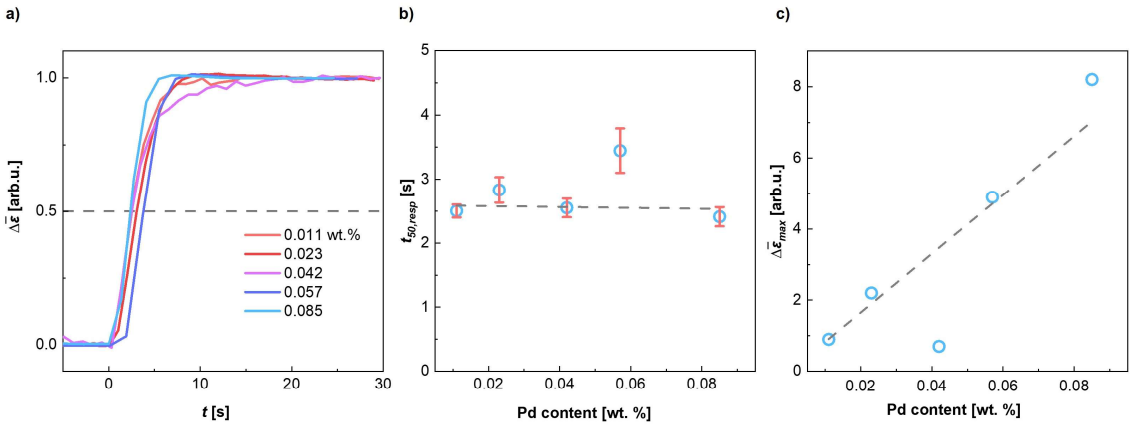

Figure 6.6. Hydrogen sensing of 100 µm thick Teflon AF:Pd plates with different Pd loading a) $\Delta\bar{\varepsilon}$ upon a stepwise increase of H_2 from 0 mbar to 100 mbar. b) Response time, $t_{50,resp}$ vs Pd content in the composites (error bars denoted the standard deviation of five measurements.) c) $\Delta\bar{\varepsilon}_{max}$ vs Pd content in the composites. Data recorded by Iwan Darmadi. Adapted from Ref.[65] Copyright American Chemical Society 2021.

This indicates that by carefully designing the hydrogen sensor, considering factors such as the matrix material, Pd content and shape and size of the sensors, it is possible to tailor the response time and sensitivity of the sensor. By the selection of the polymer with a high H_2 diffusion and limiting the sensor thickness to 100 µm the response time of the sensor is no longer affected by

the concentration of Pd particles. This enables the possibility to increase the sensitivity of the sensor by choosing a higher Pd content in the composite, without compromising the response time. This will be of relevance for operating at elevated temperatures where sensitivity of Pd-hydride based sensors tends to decrease.[133]

I 3D-printed a sensor cap with a bottom layer consisting of Teflon AF:Pd (see Chapter 5, Figure 5.3) with a Pd content of 0.023 wt. %. This sensor prototype could be combined with an optical fiber to evaluate the sensing stability. The sensor cap was exposed to 100 cycles of 4 % H_2 in synthetic air (Figure 6.7a). The 3D-printed sensor cap shows good stability and robustness during the stability test demonstrating that our sensor material could be integrated into real devices.

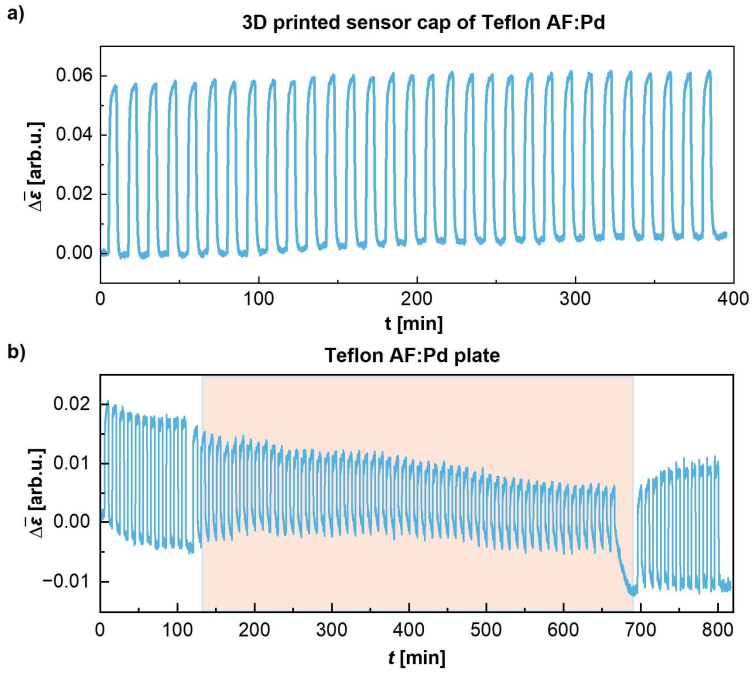

Figure 6.7. Sensor response, $\Delta\bar{\varepsilon}$, during long term stability test of a) Teflon AF:Pd 3D-printed sensor cap exposed to 4 % of H_2. b) 100 µm thick Teflon AF:Pd plate with 0.037 wt. % of Pd exposed to 5 % of H_2 and 500 ppm of CO. The orange area marks cycles containing CO. Data recorded by Iwan Darmadi. Adapted from Ref.[65] Copyright American Chemical Society 2021.

I prepared a 100 µm thick Teflon AF:Pd plate containing 0.037 wt. % of Pd in order evaluate the protective properties of the composite. The sensor was exposed to 77 cycles of 5 % H_2 in synthetic air, with 55 of these cycles containing 500 ppm of CO (Figure 6.7b). The test showed that Teflon AF does not exhibit the same protective properties as PMMA. This is due to the

large FFV of Teflon, which not only allows rapid diffusion of H_2 but also of larger molecules, including CO. The choice of a matrix polymer with a high gas diffusivity coefficient results in a sensor with a fast sensing response that however exhibits limited molecular sieving functionality.

6.4 Teflon AF:Pd coated with PMMA

The PMMA:Pd composites feature excellent stability and protective properties but have clear limitations when it comes to the H_2 sensing kinetics. Teflon AF:Pd, on the contrary, facilitates fast H_2 sensing kinetics, with a response time of a few seconds that however lacks the protective properties, which PMMA:Pd exhibits. In order to investigate if it is possible to combine both these properties in the same sensor, I prepared a series of core:shell samples comprising Teflon AF:Pd plates coated with PMMA. Based on previous results a sensor thickness of 100 μm and a Pd content of 0.037 wt. % was selected for the Teflon AF:Pd composite. The Teflon AF:Pd plates were dip coated in PMMA dissolved in anisole at different withdrawal speeds to achieve a PMMA coating thickness range from 100 to 700 nm (Complete method in Paper III).

Evaluation of the impact of the PMMA coating on the H_2 sensing kinetics was performed by exposing the sensors to a stepwise increase and decrease in H_2 ranging between 0 and 100 mbar (Figure 6.8a). Both, neat Teflon AF:Pd and PMMA coated Teflon AF:Pd had a response time $t_{50,resp} \approx$ 2-3 s and a slightly longer recovery time $t_{50,rec} \approx$ 6-8 s, demonstrating that the addition of a thin PMMA coating does not affect the sensing kinetics.

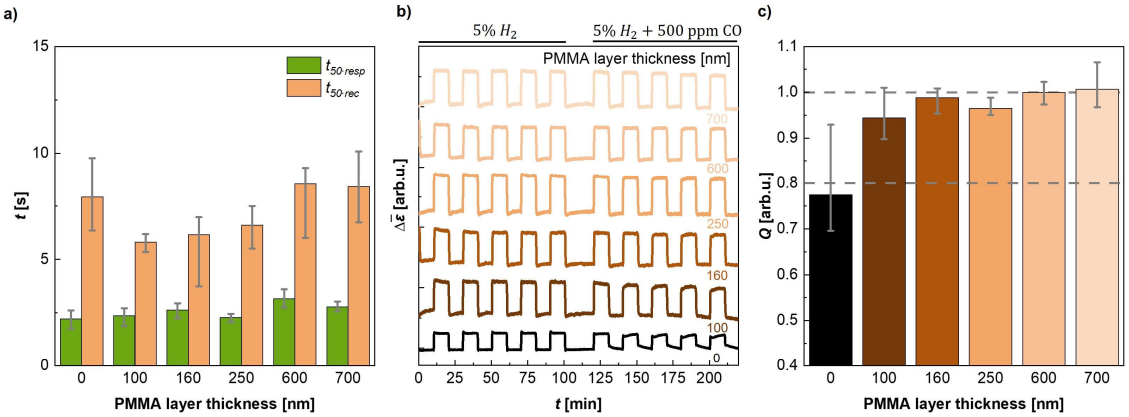

Figure 6.8. Hydrogen sensing of 100 µm thick Teflon AF:Pd plates coated with PMMA. a) Response time, $t_{50,resp}$, and recovery time, $t_{50,rec}$. b) $\Delta\bar{\varepsilon}$ upon cycling of 5 % of H_2 in synthetic air with and without the presence of 500 ppm CO. c) Quality of sensors based on Teflon AF:Pd coated with PMMA as a function of öayer thickness from sensor tests shown in (b). Error bars denote min-max values of five measurements. Data recorded by Iwan Darmadi.

In a second step the ability of the PMMA coating to protect the sensor against CO poisoning was evaluated. Teflon AF:Pd plates with and without a PMMA coating were first exposed to five cycles of H_2 in synthetic air and then exposed to five cycles of H_2 and CO in synthetic air. Teflon AF:Pd without PMMA coating slowly deactivates in the presents of CO, seen in the decay of the signal (Figure 6.8b). To evaluate the influence of CO on the sensor response, we calculated the ratio of the maximum sensor response $\Delta\bar{\varepsilon}_{max}$ during H_2 exposure before and after the introduction of CO (Figure 6.8c), here referred to as the quality factor, Q, of the sensor:

$$Q = \frac{\Delta\bar{\varepsilon}_{max,H_2+CO}}{\Delta\bar{\varepsilon}_{max,H_2}} \qquad \text{(eq. 6.3)}$$

Neat Teflon AF:Pd experiences deactivation due to CO poisoning and has a $Q = 0.77$ after five cycles containing CO, which is below the deactivation limit of ±20 % of the sensor response set by an existing performance standard for stationary H_2 sensors.[16] All coated composites show good protective properties and thus maintain a high quality of the sensor, where a coating as thin as 100 nm has a $Q = 0.94$. Increasing the coating thickness up to 600 and 700 nm resulted in the sensor achieving a $Q \approx 1$. By creating a core:shell structure composed of Teflon AF:Pd plates with a thin sub-micrometer PMMA coating, I was able to design a sensor with a fast sensor response time as well as a high degree of poisoning resistance.

6.5 Teflon AF:PdAu Composite

One challenge with Pd as the active component for hydrogen sensing is the inherent hysteresis between Pd-hydride formation and decomposition (Figure 6.9).[31, 54, 134] This reduces the accuracy of the sensor in the H_2 pressure range where the hysteresis occurs. Ideally, the sensor response should scale linearly with the H_2 pressure both during adsorption and desorption, so that a specific sensor response could directly correspond to the surrounding H_2 pressure. There are a few strategies reported on how to amend this issue such as reducing the nanoparticle size below 2.5 nm[134] or alloying of the Pd nanoparticle.[52, 135, 136]

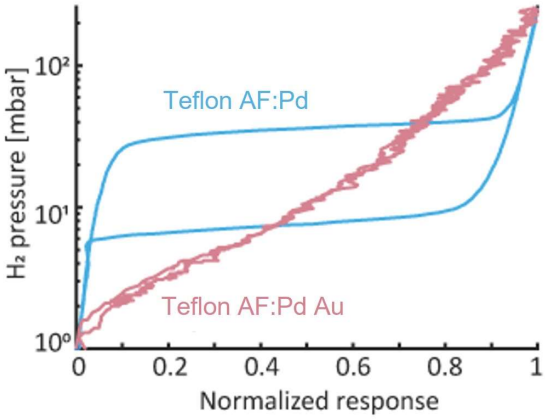

Figure 6.9. Optical pressure-composition isotherms of Teflon AF:Pd and Teflon AF:PdAu. Data recorded by Iwan Darmadi. Adapted from Ref.[63] Copyright American Chemical Society 2023.

I prepared a sample comprising Teflon AF and PdAu nanoparticles, synthesized by Sarah Lerch,[136] in order to demonstrate that the plasmonic polymer nanocomposite was compatible with Pd-alloying and that hysteresis free sensing can be achieved. The prepared Teflon AF:PdAu composite with 0.3 wt. % of PdAu nanoparticles was melt pressed into a 500 µm thick plate and evaluated by exposing it to H_2 pressure, which was slowly and stepwise increased from 0 to 300 mbar (Figure 6.9). Teflon AF:PdAu has a hysteresis free response, while Teflon AF:Pd shows clear hysteresis. This illustrates that bulk processed plasmonic polymer nanocomposites based on PdAu are suitable for the realization of accurate H_2 sensors, in line with hydrogen sensor requirements (See Chapter 1, Figure 1.2).

7. Conclusions

This thesis has explored the selection of polymers and their impact on the processability, 3D printability, and sensing properties of the corresponding plasmonic polymer nanocomposites. The optical transmittance, gas permeability and nanoparticle compatibility of the polymers as well as the polymers' ability to be melt processed were considered. A variety of plamonic plastics were produced, consisting of Au, Pd and PdAu alloy nanoparticles in combination with a wide range of polymers such as PLA, PMMA, PVDF, Dyneon THV, Hyflon AF and Teflon AF highlighting the versatility of plasmonic plastics.

Amorphous polymers showed a large potential for plasmonic polymer nanocomposites for hydrogen sensing. Thanks to their amorphous nature they exhibit a high fraction free volume, which results in a fast diffusion of hydrogen through the bulk compared to semicrystalline polymers, where the crystalline regions create a more tortuous diffusion path. In addition, amorphous polymers including PMMA, Hyflon AD and Teflon AF are a preferable choice of polymer matrix for plasmonic plastics thanks to their large optical transmittance, which does not interfere with the readout of the plasmonic peak of the nanoparticles.

To demonstrate that plasmonic plastics can be fused deposition modeling 3D-printed, replicas of the SSF- and Chalmers logo were 3D-printed with filaments of PLA:Au nanospheres and PMMA:Au nanorods as well as sensors caps of PMMA:Pd and Teflon AF:Pd. Sensor prototypes were fabricated that could be placed on an optical fiber. The possibility of transition from lab-scale to kilogram scale was assessed through the production of 2 kg of PMMA:Au nanosphere composite, that was extruded into feedstock filaments for fused deposition modeling 3D-printing. Miniature versions of the Vinga lighthouse and beacon were 3D-printed, and thus it can be concluded that a scalable processing route for 3D-printable plasmonic plastics has been developed.

In a final step, the sensing properties of the plastic plasmonic nanocomposites were evaluated. A sensor design based on PMMA:Pd resulted in a robust sensor with protective properties against poisonous gases, such as CO, and a shelf life of at least 50 weeks. The sensing kinetics were hindered by slow diffusion of hydrogen through PMMA, resulting in a long response and recovery time, which increases with sensor thickness and Pd content. Switching to the highly permeable Teflon AF as the polymer matrix and using a 100 μm thick sensor plate resulted in a short response time of 2-3 seconds. Hence, the sensors response time is no longer slowed down by the hydrogen diffusion through the polymer matrix. The selection of Teflon AF as the

polymer matrix allows to enhance the sensitivity of the sensor, by increasing the Pd content, without impacting the response time. However, the large fraction free volume of Teflon AF does not only aid hydrogen diffusion but also larger molecules such as CO, resulting in deactivation of the sensor in a CO rich environment. A core:shell structure, where Teflon AF:Pd plates are coated with a thin layer of PMMA, is found to yield a fast response time of 2-3 seconds, as well as protective properties against CO.

In summary, this thesis demonstrates the feasibility of producing plasmonic plastics that are compatible with 3D-printing. The composition and dimensions can be fined-tuned to meet specific application requirements. The primary application in this thesis was hydrogen sensing, where the polymer selection, nanoparticle composition and concentration as well as the sensor geometry could be modified to realize fast and selective optical hydrogen sensors.

8. Outlook

In my thesis I have established a robust processing route for plastic plasmonic nanocomposites, where both nanoparticles, and polymers can be altered to tailor the composites properties at the nano- and microscale.

To further improve plastic plasmonic nanocomposites used for hydrogen sensing it would be interesting to study the effect of the size of the nanoparticles. It is known that the hydrogenation kinetics are faster for smaller nanoparticles since the surface to volume ratio is larger[137], hence a decrease in nanoparticle size could further reduce the sensors response time. A nanoparticle size below 5 nm may also result in a hysteresis free sensor.[138] On the other hand, a larger nanoparticle radius increases $\Delta\bar{\varepsilon}_{max}$ of the sensor thus generating a sensor with higher sensitivity.[58, 139]

It would also be interesting to evaluate the protective properties of PMMA against other poisonous species, such as NO_x, SO_x and H_2O. Nugroho *et. al.* have previously shown that a PMMA layer of 35 nm creates a sufficient barrier against NO_x, CO_2, CH_4 and CO[28]. It would also be desirable to have the capability to study the effect of SO_x poisoning. To achieve this, it is necessary to construct a dedicated sensing system designed exclusively for detecting H_2 in the presence of SO_x, since S has the tendency to contaminate metals. Currently, there are no plasmonic hydrogen sensors that can withstand high levels of humidity. Therefore, it would be of high interest to investigate polymers with a low water permeability, such as HDPE or semi-crystalline fluoropolymers, as an additional protective coating.

To further improve the fabrication of plasmonic plastic for hydrogen sensing, it would be highly intriguing to explore co-extrusion, to generate a filament comprising a Teflon AF:Pd core and a PMMA shell. The filament could then be used directly in a 3D-printer to create various gas sensor structures with a Teflon AF:Pd bulk and a protective PMMA surface layer, making the dip coating procedure redundant.

Another intriguing approach for realisation of plasmonic plastics is to work with masterbatches that can be diluted in a subsequent processing step to tailor the concentration of the nanocomposite to the desired application. There is also the possibility to work with a multicomponent system with nanoparticles of different size, shape, or composition, resulting in different recovery times. This approach has the potential to establish a memory effect in which

the sensors not only monitor the current H_2 pressure but also retain information about past exposures.

The use of plastic plasmonic nanocomposites could be expanded to other types of sensors, by altering the nanoparticles and polymer. It could be used as an air quality sensor for NO_x by incorporating Au nanoparticles with a thin WO_3 layer[50] or CuO coated Au nanoparticles for CO sensing.[48] 3D-printing of multilayered structures, may facilitate the fabrication of an air quality sensor with the capability to detect and sense various gases simultaneously.

Nanocomposites where the plasmonic nanoparticles are accurately placed on the surface could be an interesting choice for biosensors and antimicrobial applications. This approach could also be extended to 3D-printing of highly porous scaffolds for catalysis, with the catalytic particles being located at the surface of the scaffold.

In summary, there are a lot of different opportunities to further improve plastic plasmonic nanocomposites for hydrogen sensing and to extend the concept to other applications.

9. References

1. International Energy Agency, *The Future of Hydrogen*, 2019.

2. G. W. Crabtree, M. S. Dresselhaus and M. V. Buchanan, *Phys. Today*, 2004, **57**, 39-44.

3. J. De Vrieze, K. Verbeeck, I. Pikaar, J. Boere, A. Van Wijk, K. Rabaey and W. Verstraete, *New Biotechnol.*, 2020, **55**, 12-18.

4. A. Pareek, R. Dom, J. Gupta, J. Chandran, V. Adepu and P. H. Borse, *Mater. Sci. Energy Technol.*, 2020, **3**, 319-327.

5. A. Züttel, A. Remhof, A. Borgschulte and O. Friedrichs, *Philos. Trans. R. Soc., A*, 2010, **368**, 3329-3342.

6. Hydrogen to the rescue. *Nat. Mater.*, 2018, **17**, 565-565.

7. J. X. Qian, T. W. Chen, L. R. Enakonda, D. B. Liu, G. Mignani, J.-M. Basset and L. Zhou, *Int. J. Hydrogen Energy*, 2020, **45**, 7981-8001.

8. L. Cao, I. K. M. Yu, X. Xiong, D. C. W. Tsang, S. Zhang, J. H. Clark, C. Hu, Y. H. Ng, J. Shang and Y. S. Ok, *Environ. Res.*, 2020, **186**, 109547.

9. J. Jia, L. C. Seitz, J. D. Benck, Y. Huo, Y. Chen, J. W. D. Ng, T. Bilir, J. S. Harris and T. F. Jaramillo, *Nat. Commun.*, 2016, **7**, 13237.

10. A. M. Pourrahimi, R. L. Andersson, K. Tjus, V. Ström, A. Björk and R. T. Olsson, *Sustainable Energy Fuels*, 2019, **3**, 2111-2124.

11. F. Safari and I. Dincer, *Energy Convers. Manage.*, 2020, **205**, 112182.

12. S. Dutta, *J. Ind. Eng. Chem.*, 2014, **20**, 1148-1156.

13. L. Boon-Brett, J. Bousek, G. Black, P. Moretto, P. Castello, T. Hübert and U. Banach, *Int. J. Hydrogen Energy*, 2010, **35**, 373-384.

14. T. Hübert, L. Boon-Brett, G. Black and U. Banach, *Sens. Actuators B*, 2011, **157**, 329-352.

15. U.S. Environmental Protection Agency, Criteria Air Pollutants https://www.epa.gov/criteria-air-pollutants, (accessed October 2023).

16. ISO, 26142:2010 - Hydrogen detection apparatus - Stationary applications , 2010.

17. I. Darmadi, F. A. A. Nugroho and C. Langhammer, *ACS Sens.*, 2020, **5**, 3306-3327.

18. C. Clerbaux, D. P. Edwards, M. Deeter, L. Emmons, J.-F. Lamarque, X. X. Tie, S. T. Massie and J. Gille, *Geophys. Res. Lett.*, 2008, **35**, L03817.

19. V. Palmisano, E. Weidner, L. Boon-Brett, C. Bonato, F. Harskamp, P. Moretto, M. B. Post, R. Burgess, C. Rivkin and W. J. Buttner, *Int. J. Hydrogen Energy*, 2015, **40**, 11740-11747.

20. C.-H. Han, D.-W. Hong, I.-J. Kim, J. Gwak, S.-D. Han and K. C. Singh, *Sens. Actuators, B*, 2007, **128**, 320-325.

21. M. G. Jones and T. G. Nevell, *Sens. Actuators*, 1989, **16**, 215-224.

22. R. K. Pippara, P. S. Chauhan, A. Yadav, V. Kishnani and A. Gupta, *Micro Nano Eng.*, 2021, **12**, 100086.

23. H. Yamazaki, Y. Hayashi, K. Masunishi, D. Ono and T. Ikehashi, *J. Micromech. Microeng.*, 2018, **28**, 094001.

24. R. J. Westerwaal, J. S. A. Rooijmans, L. Leclercq, D. G. Gheorghe, T. Radeva, L. Mooij, T. Mak, L. Polak, M. Slaman, B. Dam and T. Rasing, *Int. J. Hydrogen Energy*, 2013, **38**, 4201-4212.

25. J. Villatoro and D. Monzón-Hernández, *Opt. Express*, 2005, **13**, 5087-5092.

26. L. Bannenberg, H. Schreuders and B. Dam, *Adv. Funct. Mater.*, 2021, **31**, 2010483.

27. B. D. Adams and A. Chen, *Mater. Today*, 2011, **14**, 282-289.

28. F. A. A. Nugroho, I. Darmadi, L. Cusinato, A. Susarrey-Arce, H. Schreuders, L. J. Bannenberg, A. B. da Silva Fanta, S. Kadkhodazadeh, J. B. Wagner, T. J. Antosiewicz, A. Hellman, V. P. Zhdanov, B. Dam and C. Langhammer, *Nat. Mater.*, 2019, **18**, 489-495.

29. R. Jiang, F. Qin, Q. Ruan, J. Wang and C. Jin, *Adv. Funct. Mater.*, 2014, **24**, 7328-7337.

30. R. B. Schwarz and A. G. Khachaturyan, *Acta Mater.*, 2006, **54**, 313-323.

31. S. Syrenova, C. Wadell, F. A. A. Nugroho, T. A. Gschneidtner, Y. A. Diaz Fernandez, G. Nalin, D. Świtlik, F. Westerlund, T. J. Antosiewicz, V. P. Zhdanov, K. Moth-Poulsen and C. Langhammer, *Nat. Mater.*, 2015, **14**, 1236-1244.

32. I. Darmadi, F. A. A. Nugroho, S. Kadkhodazadeh, J. B. Wagner and C. Langhammer, *ACS Sens.*, 2019, **4**, 1424-1432.

33. K. M. Mayer and J. H. Hafner, *Chem. Rev.*, 2011, **111**, 3828-3857.

34. C. Langhammer, B. Kasemo and I. Zorić, *J. Chem. Phys.*, 2007, **126**.

35. I. Zorić, M. Zäch, B. Kasemo and C. Langhammer, *ACS Nano*, 2011, **5**, 2535-2546.

36. C. Langhammer, Z. Yuan, I. Zorić and B. Kasemo, *Nano Lett.*, 2006, **6**, 833-838.

37. K.-S. Lee and M. A. El-Sayed, *J. Phys. Chem. B*, 2006, **110**, 19220-19225.

38. S. S. Kalanur, Y.-A. Lee and H. Seo, *RSC Adv.*, 2015, **5**, 9028-9034.

39. J. Divya, S. Selvendran, A. S. Raja and A. Sivasubramanian, *Biosens. Bioelectron.: X*, 2022, **11**, 100175.

40. J. N. Anker, W. P. Hall, O. Lyandres, N. C. Shah, J. Zhao and R. P. Van Duyne, *Nat. Mater.*, 2008, **7**, 442-453.

41. B. Špačková, P. Wrobel, M. Bocková and J. Homola, *Proc. IEEE*, 2016, **104**, 2380-2408.

42. A. Denizli, *Plasmonic Sensors and their Applications*, Wiley, 2021.

43. C. Caucheteur, T. Guo and J. Albert, *Anal. Bioanal. Chem.*, 2015, **407**, 3883-3897.

44. N. Steinke, S. Döring, R. Wuchrer, C. Kroh, G. Gerlach and T. Härtling, *Sens. Actuators, B*, 2019, **288**, 594-600.

45. J.-F. Masson, *Analyst*, 2020, **145**, 3776-3800.

46. V. Brahmkhatri, P. Pandit, P. Rananaware, A. D'Souza and M. D. Kurkuri, *Trends Environ. Anal. Chem.*, 2021, **30**, e00117.

47. E. M. Larsson, C. Langhammer, I. Zorić and B. Kasemo, *Science*, 2009, **326**, 1091-1094.

48. A. Tittl, H. Giessen and N. Liu, *Nanophotonics*, 2014, **3**, 157-180.

49. I. B. Becerril-Castro, F. Munoz-Munoz, A. B. Castro-Ceseña, A. L. González, R. A. Alvarez-Puebla and J. M. Romo-Herrera, *Nanoscale*, 2021, **13**, 1738-1744.

50. I. Tanyeli, I. Darmadi, M. Sech, C. Tiburski, J. Fritzsche, O. Andersson and C. Langhammer, *ACS Sens.*, 2022, **7**, 1008-1018.

51. L. Chen, B. Wu, L. Guo, R. Tey, Y. Huang and D.-H. Kim, *Chem. Commun.*, 2015, **51**, 1326-1329.

52. C. Wadell, S. Syrenova and C. Langhammer, *ACS Nano*, 2014, **8**, 11925-11940.

53. F. A. A. Nugroho, P. Bai, I. Darmadi, G. W. Castellanos, J. Fritzsche, C. Langhammer, J. Gomez Rivas and A. Baldi, *Nat. Commun.*, 2022, **13**, 5737.

54. M. A. Poyli, V. M. Silkin, I. P. Chernov, P. M. Echenique, R. D. Muiño and J. Aizpurua, *J. Phys. Chem. Lett.*, 2012, **3**, 2556-2561.

55. R. Bardhan, L. O. Hedges, C. L. Pint, A. Javey, S. Whitelam and J. J. Urban, *Nat. Mater.*, 2013, **12**, 905-912.

56. A. Baldi, T. C. Narayan, A. L. Koh and J. A. Dionne, *Nat. Mater.*, 2014, **13**, 1143-1148.

57. I. Zoric´, E. M. Larsson, B. Kasemo and C. Langhammer, *Adv. Mater.*, 2010, **22**, 4628-4633.

58. F. A. A. Nugroho, I. Darmadi, V. P. Zhdanov and C. Langhammer, *ACS Nano*, 2018, **12**, 9903-9912.

59. M. Chen, P. Mao, Y. Qin, J. Wang, B. Xie, X. Wang, D. Han, G.-h. Wang, F. Song, M. Han, J.-M. Liu and G. Wang, *ACS Appl. Mater. Interfaces*, 2017, **9**, 27193-27201.

60. M. Xiao, S. Liang, J. Han, D. Zhong, J. Liu, Z. Zhang and L. Peng, *ACS Sens.*, 2018, **3**, 749-756.

61. E. Herkert, F. Sterl, N. Strohfeldt, R. Walter and H. Giessen, *ACS Sens.*, 2020, **5**, 978-983.

62. C. Sun, P. Lu, R. F. Wright and P. R. Ohodnicki, Fiber Optic Sensors and Applications XV, Proceedings of SPIE: Bellingham, WA, 2018; Vol. 10654.

63. I. Darmadi, I. Östergren, S. Lerch, A. Lund, K. Moth-Poulsen, C. Müller and C. Langhammer, *Acc. Chem. Res.*, 2023, **56**, 1850-1861.

64. I. Darmadi, A. Stolaś, I. Östergren, B. Berke, F. A. A. Nugroho, M. Minelli, S. Lerch, I. Tanyeli, A. Lund, O. Andersson, V. P. Zhdanov, M. Liebi, K. Moth-Poulsen, C. Müller and C. Langhammer, *ACS Appl. Nano Mater.*, 2020, **3**, 8438-8445.

65. I. Ostergren, A. M. Pourrahimi, I. Darmadi, R. da Silva, A. Stolas, S. Lerch, B. Berke, M. Guizar-Sicairos, M. Liebi, G. Foli, V. Palermo, M. Minelli, K. Moth-Poulsen, C. Langhammer and C. Muller, *ACS Appl. Mater. Interfaces*, 2021, **13**, 21724-21732.

66. J. Hong, S. Lee, J. Seo, S. Pyo, J. Kim and T. Lee, *ACS Appl. Mater. Interfaces*, 2015, **7**, 3554-3561.

67. P. Ngene, R. J. Westerwaal, S. Sachdeva, W. Haije, L. C. P. M. de Smet and B. Dam, *Angew. Chem., Int. Ed.*, 2014, **53**, 12081-12085.

68. K.-J. Jeon, H. R. Moon, A. M. Ruminski, B. Jiang, C. Kisielowski, R. Bardhan and J. J. Urban, *Nat. Mater.*, 2011, **10**, 286-290.

69. Transfer Multisort Elektronik, PMMA 1,75 TRANSPARENT DEVIL DESIGN, https://www.tme.eu/se/details/dev-pmma-1.75-tra/3d-skrivare-och-tillbehor/devil-design/pmma-1-75-transparent/, (accessed 2023-10-23).

70. 3D Prima, Filament, https://www.3dprima.com/se/filament-resin/filament, (accessed 2023-10-23).

71. Simplify 3D, Materials guide - PLA, https://www.simplify3d.com/resources/materials-guide/pla/, (accessed 2023-10-23).

72. Z. Cui, E. Drioli and Y. M. Lee, *Progress in Polymer Science*, 2014, **39**, 164-198.

73. H. Teng, *Applied Sciences*, 2012, **2**, 496-512.

74. M. B. Karimi, F. Mohammadi and K. Hooshyari, *Int. J. Hydrogen Energy*, 2019, **44**, 28919-28938.

75. F. Liu, B. Yi, D. Xing, J. Yu and H. Zhang, *J. Membr. Sci.*, 2003, **212**, 213-223.

76. M. Minelli and G. C. Sarti, *Membranes*, 2018, **8**.

77. M. Minelli and G. C. Sarti, *Fluid Phase Equilib.*, 2016, **424**, 44-51.

78. M. Minelli and G. C. Sarti, *J. Membr. Sci.*, 2017, **521**, 73-83.

79. Ansys GRANTA EduPack software, ANSYS, Inc., Cambridge, UK, YEAR (www.ansys.com/materials). (accessed 2023-10-30)

80. L. W. McKeen, in *Permeability Properties of Plastics and Elastomers (Fourth Edition)*, ed. L. W. McKeen, William Andrew Publishing, 2017, pp. 157-207.

81. Y. Sun, H. Lv, W. Zhou and C. Zhang, *Int. J. Hydrogen Energy*, 2020, **45**, 24980-24990.

82. L. W. McKeen, in *Permeability Properties of Plastics and Elastomers (Fourth Edition)*, ed. L. W. McKeen, William Andrew Publishing, 2017, pp. 129-155.

83. A. Ghassemi, S. Moghaddamzadeh, C. Duchesne and D. Rodrigue, *J. Plast. Film Sheeting*, 2017, **33**, 361-383.

84. L. W. McKeen, in *Permeability Properties of Plastics and Elastomers (Fourth Edition)*, ed. L. W. McKeen, William Andrew Publishing, 2017, pp. 305-323.

85. Solvay Solexis. Solef & Hylar PVDF Design and Processing Guide. (2006).

86. L. W. McKeen, in *Permeability Properties of Plastics and Elastomers (Fourth Edition)*, ed. L. W. McKeen, William Andrew Publishing, 2017, pp. 249-287.

87. The Chemours Company. *Teflon AF Product Information*. (20

88. 3M. *3M Dyneon Product Data Sheet*. (2013).

89. Solvay Specialty Polymers. *Solvene 250 EAP Technical Data Sheet*. (2015).

90. J. D. Carrico, N. W. Traeden, M. Aureli and K. K. Leang, *Smart Mater. Struct.*, 2015, **24**, 125021.

91. S. Clémenson, E. Espuche, L. David and D. Léonard, *J. Membr. Sci.*, 2010, **361**, 167-175.

92. W. Wang, S. Zhang, L.-o. Srisombat, T. R. Lee and R. C. Advincula, *Macromol. Mater. Eng.*, 2011, **296**, 178-184.

93. A. M. Pourrahimi, T. A. Hoang, D. Liu, L. K. H. Pallon, S. Gubanski, R. T. Olsson, U. W. Gedde and M. S. Hedenqvist, *Adv. Mater.*, 2016, **28**, 8651-8657.

94. A. Soroudi, Y. Ouyang, F. Nilsson, I. Östergren, X. Xu, Z. Li, A. M. Pourrahimi, M. Hedenqvist, T. Gkourmpis, P.-O. Hagstrand and C. Müller, *Nanoscale*, 2022, **14**, 7927-7933.

95. I. Khan, I. Khan, K. Saeed, N. Ali, N. Zada, A. Khan, F. Ali, M. Bilal and M. S. Akhter, in *Smart Polymer Nanocomposites*, eds. N. Ali, M. Bilal, A. Khan, T. A. Nguyen and R. K. Gupta, Elsevier, 2023, pp. 167-184.

96. Y. Xia, Y. Xiong, B. Lim and S. E. Skrabalak, *Angew. Chem., Int. Ed.*, 2009, **48**, 60-103.

97. S. Sacanna, M. Korpics, K. Rodriguez, L. Colón-Meléndez, S.-H. Kim, D. J. Pine and G.-R. Yi, *Nat. Commun.*, 2013, **4**, 1688.

98. W. Niu, Z.-Y. Li, L. Shi, X. Liu, H. Li, S. Han, J. Chen and G. Xu, *Cryst. Growth Des.*, 2008, **8**, 4440-4444.

99. A. Pekkari, Z. Say, A. Susarrey-Arce, C. Langhammer, H. Härelind, V. Sebastian and K. Moth-Poulsen, *ACS Appl. Mater. Interfaces*, 2019, **11**, 36196-36204.

100. A. Stolaś, I. Darmadi, F. A. A. Nugroho, K. Moth-Poulsen and C. Langhammer, *ACS Appl. Nano Mater.*, 2020, **3**, 2647-2653.

101. C. G. G. Zehev Tadmor, *Principles of Polymer Processing*, John Wiley & Sons, Inc.,, Hoboken, New Jersey, 2nd edn., 2006.

102. J.-Z. Liang, J. Yang and C.-Y. Tang, *Polym. Test.*, 2010, **29**, 624-628.

103. P. K. Penumakala, J. Santo and A. Thomas, *Composites, Part B*, 2020, **201**, 108336.

104. L. Wang, M. Hasanzadeh Kafshgari and M. Meunier, *Adv. Funct. Mater.*, 2020, **30**, 2005400.

105. Y. Lin, E. Bilotti, C. W. M. Bastiaansen and T. Peijs, *Polym. Eng. Sci.*, 2020, **60**, 2351-2376.

106. S. Link and M. A. El-Sayed, *J. Phys. Chem. B*, 1999, **103**, 4212-4217.

107. H.-H. Chang and C. J. Murphy, *Chem. Mater.*, 2018, **30**, 1427-1435.

108. H. Chen, L. Shao, Q. Li and J. Wang, *Chem. Soc. Rev.*, 2013, **42**, 2679-2724.

109. T. Pradeep, in *Textbook of Nanoscience and Nanotechnology*, McGraw-Hill Education, New York, 2012.

110. N. Emami, M. Sjödahl and K.-J. M. Söderholm, *Dent. Mater.*, 2005, **21**, 721-730.

111. L. W. McKeen, in *Permeability Properties of Plastics and Elastomers (Fourth Edition)*, ed. L. W. McKeen, William Andrew Publishing, 2017, pp. 1-19.

112. M. Giacinti Baschetti and M. Minelli, *Polym. Test.*, 2020, **89**, 106606.

113. ASTM International, D1434-82 - Standard Test Method for Determining Gas Permeability Characteristics of Plastic Film and Sheeting, 2023.

114. J. Crank, *The Mathematics of Diffusion*, Clarendon press, Oxford, Second edn., 1979.

115. M. Minelli, M. G. De Angelis, F. Doghieri, M. Marini, M. Toselli and F. Pilati, *Eur. Polym. J.*, 2008, **44**, 2581-2588.

116. M. C. Ferrari, M. Galizia, M. G. De Angelis and G. C. Sarti, *Ind. Eng. Chem. Res.*, 2010, **49**, 11920-11935.

117. G. M. Insights, *Polymer Nanocomposites Market - By Polymer (Epoxy Resin, Polyamide, Polyethylene, Polypropylene), By Nanomaterials (Nanoclays, Carbon Nanotubes, Nanofibers, Nano-oxides) and End-user Industry & Forecast, 2022-2028*, https://www.gminsights.com/toc/detail/polymer-nanocomposites-market, (accessed 2023-10-30)

118. A. Pekkari, PhD thesis, Colloidal synthesis of metal nanoparticles, Chalmers University of Technology, 2020.

119. D. W. R. Ian Gibson, Brent Stucker, *Additive Manufacturing Technologies - Rapid Prototyping to Direct Digital Manufacturing*, Springer New York, NY, New York, NY, 1st edn., 2010.

120. O.-A. Denisse and M. Tanya, in *Functional Materials*, ed. S. Dipti, IntechOpen, Rijeka, 2018, p. Ch. 1.

121. B. N. Turner, R. Strong and S. A. Gold, *Rapid Prototyp. J.*, 2014, **20**, 192-204.

122. T. D. Ngo, A. Kashani, G. Imbalzano, K. T. Q. Nguyen and D. Hui, *Composites, Part B*, 2018, **143**, 172-196.

123. B. P. Conner, G. P. Manogharan, A. N. Martof, L. M. Rodomsky, C. M. Rodomsky, D. C. Jordan and J. W. Limperos, *Addit. Manuf.*, 2014, **1-4**, 64-76.

124. M. Carrola, A. Asadi, H. Zhang, D. G. Papageorgiou, E. Bilotti and H. Koerner, *Adv. Funct. Mater.*, 2021, **31**, 2103334.

125. Protopasta, Conductive PLA, https://proto-pasta.com/pages/conductive-pla, (accessed 2023-10-24).

126. 3D Compare, Black Magic 3D Conductive Graphene Composite 1.75 mm, https://3dcompare.com/materials/product/black-magic-3d-conductive-graphene-composite-1-75-mm/, (accessed 2013-10-24).

127. Copper3D, Antimicrobial Performance, https://copper3d.com/pages/antimicrobial-performance, (accessed 2023-10-24).

128. L. Kool, A. Bunschoten, A. H. Velders and V. Saggiomo, *Beilstein J. Nanotechnol.*, 2019, **10**, 442-447.

129. A. P. Haring, A. U. Khan, G. Liu and B. N. Johnson, *Adv. Opt. Mater.*, 2017, **5**, 1700367.

130. Y. Xu, X. Wu, X. Guo, B. Kong, M. Zhang, X. Qian, S. Mi and W. Sun, *Sensors*, 2017, **17**, 1166.

131. Simplify3D, Print Quality Troubleshooting - Warping, https://www.simplify3d.com/resources/print-quality-troubleshooting/warping/, (accessed 2023-10-24).

132. P. Chen, N. T. Tran, X. Wen, Q. Xiong and B. Liedberg, *ACS Sens.*, 2017, **2**, 235-242.

133. M. Fisser, R. A. Badcock, P. D. Teal and A. Hunze, *Sens. Actuators, B*, 2018, **259**, 10-19.

134. C. Langhammer, V. P. Zhdanov, I. Zorić and B. Kasemo, *Chem. Phys. Lett.*, 2010, **488**, 62-66.

135. C. Wadell, F. A. A. Nugroho, E. Lidström, B. Iandolo, J. B. Wagner and C. Langhammer, *Nano Lett.*, 2015, **15**, 3563-3570.

136. S. Lerch, A. Stolaś, I. Darmadi, X. Wen, M. Strach, C. Langhammer and K. Moth-Poulsen, *ACS Appl. Mater. Interfaces*, 2021, **13**, 45758-45767.

137. C. J. Brinker, in *Chemical Solution Deposition of Functional Oxide Thin Films*, eds. T. Schneller, R. Waser, M. Kosec and D. Payne, Springer Vienna, Vienna, 2013 , pp. 233-261.

138. A. Pundt, M. Suleiman, C. Bähtz, M. T. Reetz, R. Kirchheim and N. M. Jisrawi, *Mater. Sci. Eng. B*, 2004, **108**, 19-23.

139. K. J. Palm, J. B. Murray, T. C. Narayan and J. N. Munday, *ACS Photonics*, 2018, **5**, 4677-4686.